

**DOKUZ EYLÜL UNIVERSITY**  
**GRADUATE SCHOOL OF NATURAL AND APPLIED SCIENCES**

**APPLICATION OF PROBABILISTIC MODELLING  
ANALYSIS AND FILTERING INTO IMAGE  
SEGMENTATION**

**by**  
**Merve ÖZDEMİR**

**February, 2015**  
**İZMİR**

# **APPLICATION OF PROBABILISTIC MODELLING ANALYSIS AND FILTERING INTO IMAGE SEGMENTATION**

**A Thesis Submitted to the  
Graduate School of Natural and Applied Sciences of Dokuz Eylül University  
In Partial Fulfillment of the Requirements for the Master of Science of  
Electrical and Electronics Engineering**

**by  
Merve ÖZDEMİR**

**February, 2015  
İZMİR**

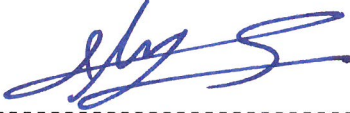
## M.Sc. THESIS EXAMINATION RESULT FORM

We have read the thesis entitled “**APPLICATION OF PROBABILISTIC MODELLING ANALYSIS AND FILTERING INTO IMAGE SEGMENTATION**” completed by **MERVE ÖZDEMİR** under supervision of **DOÇ. DR. OLCAY AKAY** and we certify that in our opinion it is fully adequate, in scope and in quality, as a thesis for the degree of Master of Science.




Doç. Dr. OLCAY AKAY

Supervisor



Yrd. Doç. Dr. M. Alper SELVER

(Jury Member)



Prof. Dr. Oğuz DİCLE

(Jury Member)



Prof. Dr. Ayşe OKUR  
Director

Graduate School of Natural and Applied Science

## **ACKNOWLEDGMENTS**

I would like to thank my supervisor, Assoc. Prof. Dr. Olcay Akay, for his patience, confidence, encouragement, and valuable suggestions.

I would like to thank Asst. Prof Dr. M. Alper Selver for providing me with the opportunity to work in his research project and supporting me with his valuable knowledge and suggestions during my thesis work. I also would like to thank my committee member, Prof. Dr. Oğuz Dicle, for sharing his valuable suggestions during my thesis work and the research project.

I also would like to thank my colleague Eşref Selvi for his undying patience, encouragement, and support. I appreciate my dear friend Onur Akinönder for his valuable and helpful emotional support. Finally, I would like to thank my family for their patience and sensibilities.

This thesis was supported by TÜBİTAK under grant number 112E032.

Merve ÖZDEMİR

# APPLICATION OF PROBABILISTIC MODELLING ANALYSIS AND FILTERING INTO IMAGE SEGMENTATION

## ABSTRACT

In the generation of volume rendered images, Transfer Function (TF) specification has an important role. The specification of an appropriate TF that allows intuitive control of the visual parameters is a very challenging task. In Magnetic Resonance Imaging (MRI), this process is even harder since certain types of volume data are not standardized in pre-defined range of data values. Based on the MRI sequence in use and depending on the acquisition parameters, data specific sub-ranges might be assigned to the same type of structure. To be able to work in all possible cases, automatic sub-range detection methods are required. In this study, a semi-automatic method for initial generation of TFs is introduced.

Our approach is based on Volume Histogram Stack (VHS) which is created by re-generating the image slices of a dataset based on a user specified spline. VHS is obtained by aligning the histograms of the image slices of the MRI series. By considering the VHS structure, Gaussian basis functions provide a good approximation for fitting the lobes of the VHS. Approximating the VHS using Gaussian basis functions allows a coarse classification and enables an effective initial TF design. The developed technique employs hierarchical approximation of the VHS using Gaussians with multiple orientations and scales. Then, a finer classification step is carried out for refinement of the initial result. As a finer classification, which is based on spatial domain knowledge, such morphological operations as dilation, and erosion and region growing are applied. The proposed method is applied to 29 (14 T1 DUAL+10 T1 WATS+5 THRIVE) MRI datasets for abdominal tissue/organ visualization. The results show that the proposed system provides a useful and intuitive initialization for TF design. Applications to several MRI datasets testify the success of the developed technique in accurate visualization of abdominal tissues/organs.

**Keywords:** MRI, TF specifications, volume histogram stacks, volume rendering

# RASSAL MODELLEME ANALİZ VE FİLTRELEMENİN GÖRÜNTÜ BÖLÜTLEMESİNE UYGULANMASI

## ÖZ

Transfer Fonksiyon (TF) belirleme, hacimsel işlenmiş görüntüleri elde etmede önemli bir role sahiptir. Görsel parametreleri sezgisel olarak kontrol etmeye yarayan uygun bir TF belirleme oldukça zor bir iştir. Bu işlem Manyetik Rezonans Görüntüleme (MRG) için daha zordur çünkü türü belli olan hacim verileri önceden tanımlanmış bir aralıkta standardize edilmemiştir. Kullanılan MRG sekanslarına ve edinim parametrelerine göre belirli alt aralıklar aynı tip yapı olarak atanabilir. Bütün olası durumlarda çalışabilmesi için, otomatik alt aralık belirleme yöntemleri gereklidir. Bu çalışmada, ilk TF üretimi için yarı-otomatik bir yöntem tanıtılmaktadır.

Bizim yaklaşımımız kullanıcı tarafından belirlenen şeride göre yeni görüntü dilimleri üretmeye dayalı olan Hacim Histogram Yığını'nın (HHY) oluşturulması temel alınarak yapılmıştır. HHY, MRG serisinin görüntü dilimlerini sıralayarak elde edilir. HHY yapısını dikkate alırsak, Gauss fonksiyonları HHY loblarının belirlenmesinde iyi bir yaklaşık değer sağlar. Gauss fonksiyonlarını kullanarak HHY'ye yakınsamak, kabaca bir sınıflama yapmayı ve etkili bir ilk TF elde edilmesini sağlar. Geliştirilen teknik, Gauss temelli çoklu yönelim ve ölçekleme kullanarak sıradüzenli bir yaklaşım kullanmaktadır. Daha sonra, ilk sonuçları daha da iyileştirmek için detaya inen bir belirleme adımı geliştirilmiştir. Uzaysal etki alanı bilgisi temelli iyi sınıflama için genişletme ve erozyon gibi morfolojik operasyonlar ve bölge büyütme teknikleri uygulanmıştır. Önerilen yöntem, abdomen doku/organ gösterimi için 29 (14 T1 DUAL+10 T1 WATS+5 THRIVE) MRG veri setine uygulanmıştır. Sonuçlar, TF tasarımı için önerilen sistemin kullanışlı ve sezgisel bir başlatma sağladığını göstermektedir. Çeşitli MRG veri setlerine uygulanma sonuçları, önerilen yöntemin abdomen bölgeye ait dokuların/organların doğru gösterimlerini elde etmedeki başarısını göstermektedir.

**Anahtar Kelimeler:** MRG, TF belirtilmeleri, hacimsel histogram yığınları, hacimsel imge oluşturma

## CONTENTS

	Page
M.Sc. THESIS EXAMINATION RESULT FORM.....	ii
ACKNOWLEDGMENTS .....	iii
ABSTRACT.....	iv
ÖZ .....	v
LIST OF FIGURES .....	viii
LIST OF TABLES .....	xii
 <b>CHAPTER ONE - INTRODUCTION .....</b>	 <b>1</b>
 <b>CHAPTER TWO - MAGNETIC RESONANCE IMAGING AND MR DATASET.....</b>	 <b>6</b>
2.1 Magnetic Resonance Imaging (MRI).....	6
2.1.1 What is an MRI Scan? .....	7
2.2 MRI Sequences.....	8
2.2.1 MRI Sequences Process.....	10
2.2.2 Classification of MRI Sequences.....	11
2.3 Slice Thickness and Spacing .....	14
2.4 Datasets .....	14
 <b>CHAPTER THREE - GENERATION OF ARBITRARILY ALIGNED VOLUME HISTOGRAM STACK (VHS).....</b>	 <b>17</b>
3.1 Anatomical Planes .....	17
3.1.1 Frontal (Coronal) Plane .....	17
3.1.2 Sagittal (Lateral) Plane .....	18
3.1.3 Transverse (Axial) Plane .....	18
3.1.4 Oblique Planes .....	19

3.2 Developed Graphical User Interface (GUI) .....	20
3.2.1 User Guide of the GUI.....	21
3.3 Computation of VHS .....	29
3.3.1 The Interaction between the GUI and VHS.....	33
 <b>CHAPTER FOUR - GAUSSIAN APPROXIMATION MODEL.....</b>	<b>38</b>
4.1 Gaussian Function .....	38
4.2 Approximation of VHS via Gaussian Functions.....	39
4.2.1 Gaussian Parameters and Orientations .....	41
4.2.2 Implementation of Gaussian Approximation Model .....	45
4.2.3 The Thresholding Process.....	51
4.2.4 Morphological Operations .....	52
4.2.4.1 Implementation of the Morphological Operations.....	53
4.2.5 Region Growing.....	55
 <b>CHAPTER FIVE - APPLICATION AND RESULTS .....</b>	<b>57</b>
5.1 General Overview.....	68
 <b>CHAPTER SIX - CONCLUSION .....</b>	<b>69</b>
 <b>REFERENCES.....</b>	<b>72</b>



## LIST OF FIGURES

Figure 2.1 Extent of the 0.5 mTesla (mT) fringe field around a 1.5 Tesla (T); (Courtesy of Philips Medical Systems).....	7
Figure 2.2 (a) Coronal image of the brain showing a tumor. In this image, the tumor is bright against the darker grey of the normal brain tissue. (b) The same slice with a different pulse sequence, this time showing the tumor darker than the surrounding brain tissue. ....	9
Figure 2.3 The basics of MRI (a) The tissues have different proton densities and 90° pulse is applied. (b) A 90° pulse knocks both magnetizations into the transverse plane where they create a signal. (c) After some time signal has decayed to zero while $M_z$ recovers. (d) When the second 90° pulse is applied after time TR, reduced signals are rotated into the transverse plane. (e) After another TR, both $M_z$ have recovered to the same height as before. (f) The third 90° pulse creates the same T1-weighted signal in the transverse plane. ....	10
Figure 2.4 The classification of echoes.....	11
Figure 2.5 Different image slices of T2-SPIR sequence.....	12
Figure 2.6 Different image slices of T1-DUAL sequence .....	13
Figure 2.7 Different image slices of SSH sequence.....	13
Figure 2.8 Different image slices of THRIVE sequence .....	14
Figure 3.1 (a) Different anatomical planes of the human body, (b) imaging of different anatomical planes. ....	17
Figure 3.2 General overview of the different planes (a) axial, (b) coronal, and (c) sagittal plane.....	18
Figure 3.3 Different slices from axial plane.....	19
Figure 3.4 Oblique plane selection obtained from other planes.....	20
Figure 3.5 Address selection of the GUI.....	22
Figure 3.6 Axial, coronal, and sagittal plane images of the interface .....	23
Figure 3.7 Line selection with respect to selected surface plane. Surface selection is from axial plane. Line selection is in (a) coronal plane and (b) sagittal	

plane. Surface selection is from coronal plane. Line selection is in (c) axial plane and (d) sagittal plane. Surface selection is from sagittal plane. Line selection is in (e) axial plane and (f) coronal plane. ....	25
Figure 3.8 (a) Reconstruction strategy inside the volume, (b) circular area selection from axial, (c) vertical height selection from sagittal (left kidney) .....	26
Figure 3.9 Ellipse area selection from (a) axial, (b) coronal, and (c) sagittal plane ..	27
Figure 3.10 Reconstruction strategy inside the volume for rectangular area.....	27
Figure 3.11 Rectangular area selection from (a) axial, (b) coronal, and (c) sagittal plane .....	28
Figure 3.12 Spline selection on liver (a) axial plane, (b) coronal plane, (c) sagittal planes.....	29
Figure 3.13 MPR images which are obtained from (a) axial, (b) coronal, and (c) sagittal planes .....	29
Figure 3.14 Gray levels and shape variations in the kidneys.....	30
Figure 3.15 Gray levels and shape variations in the liver.....	30
Figure 3.16 Gray levels and shape variations in the spleen .....	30
Figure 3.17 (a) Aligning the histograms of the image slices of an MR series, (b) an example of VHS. ....	32
Figure 3.18 (a) MPR images obtained from the GUI, (b) the benchmark data of the reconstructed images .....	34
Figure 3.19 Ellipse is selected from the axial plane and the height is selected from the coronal plane. ....	35
Figure 3.20 Ellipse is selected from the axial plane and the height is selected from the coronal plane with a different VHS view.....	35
Figure 3.21 Spline is selected from the axial plane and the height is selected from the coronal plane .....	36
Figure 3.22 Spline is selected from the axial plane and the height is selected from the coronal plane with a different VHS view .....	36
Figure 3.23 (a) VHS of MPR images which are obtained via splines, (b) desired histogram of the obtained MPR .....	37
Figure 4.1 A 2-D Gaussian curve.....	39

Figure 4.2 (a)-(c) Top view of resultant VHS of the GUI (d)-(f) Top view of their respective desired counterparts. ....	40
Figure 4.3 2-D Gaussian functions with respect to different angles (a)-(c) Top view (d)-(f) Side view. ....	42
Figure 4.4 Filterbank of Gaussian basis functions (each row corresponds to a certain scale and each column corresponds to a certain orientation) .....	43
Figure 4.5 Each labeled part of (a-h) represents residual correlation between VHS and the Gaussian kernel in different scales after fitting with an appropriate filter size and angle. (i) Final approximation with all Gaussian functions. ....	50
Figure 4.6 (a) The resultant approximating Gaussian functions (b) Top view of the resultant approximation of Gaussian functions with a varying threshold range represented by red lines. ....	51
Figure 4.7 The flowchart of the Gaussian modelling process.....	52
Figure 4.8 Implementation of the structuring element in an image. ....	53
Figure 4.9 3-D structuring element as observed from different angles.....	55
Figure 5.1 MPR images belonging to T1 WATS with slice numbers (a) 3-11-21 and (b) 2-13-21. MPR images belonging to T1-DUAL with slice numbers (c) 12-18-24 and (d) 2-10-22. ....	58
Figure 5.2 Different axial image slices belonging to T1 DUAL before morphological operations. ....	60
Figure 5.3 Different axial image slices belonging to T1 WATS before morphological operations. ....	61
Figure 5.4 Different axial image slices belonging to THRIVE before morphological operations. ....	61
Figure 5.5 Different axial image slices belonging to T1 DUAL after morphological operations. ....	63
Figure 5.6 Different axial image slices belonging to T1 WATS after morphological operations. ....	63
Figure 5.7 Different axial image slices belonging to THRIVE after morphological operations. ....	63

Figure 5.8 Different axial image slices belonging to T1 DUAL after region growing.	66
Figure 5.9 Different axial image slices belonging to T1 WATS after region growing.	66
Figure 5.10 Different axial image slices belonging to THRIVE after region growing.	66

## LIST OF TABLES

	<b>Page</b>
Table 2.1 The list of the datasets and the MRI sequences used in this study (mm). .	16
Table 5.1 <i>VOE</i> results with respect to MR sequences .....	60
Table 5.2 Metric results of T1 DUAL sequence with respect to the dataset .....	61
Table 5.3 Metric results of T1 WATS sequence with respect to the dataset .....	62
Table 5.4 Metric results of THRIVE sequence with respect to the dataset .....	62
Table 5.5 Metric results of T1 DUAL sequence after morphological operations with respect to the dataset .....	65
Table 5.6 Metric results of T1 WATS sequence after morphological operations with respect to the dataset .....	65
Table 5.7 Metric results of THRIVE sequence after morphological operations with respect to the dataset .....	65
Table 5.8 Metric results of T1 DUAL sequence after region growing with respect to the dataset.....	67
Table 5.9 Metric results of T1 WATS sequence after region growing with respect to the dataset.....	67
Table 5.10 Metric results of THRIVE Sequence after region growing with respect to the dataset.....	67
Table 5.11 Comparison of the average metric results of all sequences after region growing.....	68

## **CHAPTER ONE**

### **INTRODUCTION**

Volume rendering has a crucial role in scientific visualization of large amounts of data. Medical modalities such as Computed Tomography (CT) and Magnetic Resonance Imaging (MRI) create a volume data by acquiring a series of cross sections of the anatomy of interest. The visualization of this three dimensional (3-D) data can help many scientific disciplines in addition to slice-by-slice evaluation of two dimensional (2-D) data. Instead of dealing with 2-D data, physicians (i.e. surgeons, oncologists) prefer 3-D data, which provides more effective and intuitive visualizations for applications such as surgery planning, treatment follow-ups, and education. Thus, it can be clearly stated that, for visualizing the interior structure of the body, the volumetric data is becoming more and more preferable than viewing a series of images (Drebin, Carpenter, & Hanrahan, 1988).

During the recent decades, rendering and visualization systems have been developed to handle more complex problems. Besides these developments, one of the major goals of medical visualization is to express clear and informative images of a dataset. Identifying correct visual information of tissues and organs of interest still remains as a difficult and time-consuming task for many medical applications. This is also related to opacity and color assignments, which should be determined interactively to fulfill the expectations of the physician (Kindlman & Durkin, 1998). During the generation of volume rendered images, Transfer Function (TF) specification is the crucial step at which these visual parameters are defined (Levoy, 1988; Sabella, 1988; Upson & Keeler, 1988). Therefore, determination of the optical parameters by using a TF is an important step to construct a valuable outcome in rendering. As a result, being an element of the rendering pipeline, specification of an appropriate TF is a tedious but also a crucial task to produce meaningful 3-D images (König & Gröller, 2001; Pfister et al., 2000; Pfister et al., 2001).

One of the reasons behind the difficulty of TF design is the empirical structure of its domain. Extensive search spaces are available for TFs, but there are still ongoing research activities that are necessary for generating more effective domains. Usually, the domain of a TF enables its initial design, which provides a starting point prior to the optimization that is controlled by the user. To overcome the difficulty of initial TF generation, generally a number of predefined TF presets are used (Kniss, Kindlmann, & Hansen, 2002). The main idea behind this approach is that certain types of volume data are standardized in the range of data values and special sub-ranges are assigned to the same type of structure. Thus, predefined TFs can be adjusted according to these ranges (Lundström, Ljung, & Ynnerman, 2006a; 2006b). However, in MRI, volumetric data usually have varying characteristics due to acquisition parameters, artifacts, field inhomogeneity, and characteristics of different sequences. In those cases, a limited number of TFs is not enough and automatic sub-range detection methods are needed. Accordingly, in this study, a semi-automatic method for initial generation of TFs is introduced.

In clinic, the segmented image series are labeled by using appropriate software tools under the control of an expert. Unfortunately, image series include a large number of slices making this task time consuming and burdensome. To ease the delineation of the images, some recent segmentation algorithms are introduced which consist of semi-automatic and automatic techniques. There are mainly two approaches for segmenting a series of medical images:

- 1) 3-D approaches which use 3-D information provided by volumetric data constructed by integration of image slices (Bidaut, 2000).
- 2) Slice-by-slice (or iterative 2-D) approaches which perform segmentation on a single image but use adjacent slice information in some manner (Koss, Newman, Johnson, & Kirch, 1999; Lee, Chung, & Tsai, 2003; Selver et al., 2008).

Although, organs of interest are 3-D in nature, the use of first approach (i.e. 3-D models and/or features) requires a large number of training shapes/data which are not

available for objects that can vary largely (i.e. most of the organs). Moreover, the high anisotropy of CT and MRI data makes intra-slice information more reliable than inter-slice features, which must be extracted after an interpolation process. Furthermore, the results of 3-D algorithms are also in 3-D, preventing easy transition to 2-D images which experts use to make final modifications on the segmentation result.

The second approach (i.e. slice-by-slice analysis) has the advantage of complete integration with the current manual segmentation schemes. These methods should combine 2-D segmentation with appropriate slice similarity features. If an effective similarity measure is used such methods can become computationally feasible even for a large number of slices. The drawbacks of 3-D approaches can also be avoided (Bidaut, 2000; Selver et al., 2008).

Segmentation has an important role in medical imaging for classification and visualization of similar tissues. Medical imaging such as CT and MRI can represent a part of the body by a large number of image slices with an inner thickness of each slice. Segmentation is a vital task because the grey-scales of different organs and non-object tissues are not identical and overlapping with each other. To obtain an efficient segmentation in the extraction of a considered tissue or organ from the body, both performance and computational complexity of the segmentation process must be taken into account, since there is an apparent trade-off between complexity and accuracy of any segmentation method (Bidaut, 2000).

As mentioned before, dealing with medical imaging has an important and beneficial role in facilitating the clinical field, although it also has some difficulties. By now, various recent studies have introduced new approaches about segmentation of organs which lie in different parts of the body. Abdomen region is one of the most challenging regions to segment in the body, because it contains many organs and has a complex structure with similar grey-levels of adjacent organs and the outer region. By far, segmentation in the abdomen region is generally considered for CT images (Bae, Giger, Chen, & Jr. Kahn, 1993). MRI is not preferred as much as CT. The



drawback of using the MRI is the fact that it is affected more by the complexity of the abdominal region and it has a low gradient response (Chen, Gu, Qian, & Xu, 2009).

Here, it is worth to point out that there are many (semi) automatic segmentation techniques, which rely on segmenting the anatomy first, and then applying existing volume rendering to the segmented data for 3-D analysis. This is a very critical issue concerning the use of complicated TF techniques instead of performing segmentation. The reason behind preferring TF design instead of segmentation is the fact that in most of the cases, what is interesting from clinical point of view is usually not only an organ or tissue itself, but also its properties together with adjacent organs or related vessel systems that are coming into and going out of it. Thus, the limitation of the segmentation is that it results only with the object of interest. Even if the segmentation is perfectly done, it is not possible to render it together with the adjacent tissues/organs and/or incoming/outgoing vascular trees etc., unless another segmentation process is performed for each object of interest. On the other hand, TF specification has the advantage that the user can have all the volumetric data at all times. More informative renderings can produce multiple anatomical structures at the same time and that is why this thesis focuses on developing more advanced TF specification techniques instead of concentrating on segmentation.

Our approach in this thesis for segmentation is based on a Volume Histogram Stack (VHS) which is created by aligning the histograms of the image slices of MR series. However, VHS is not calculated directly using the acquired image slices. By considering the challenging structure of the MRI, a new interface is introduced which constructs new slices by using different planes of the 3-D image matrix. Before aligning the histograms, new slices are generated by the user. The user draws a certain shape (line, rectangle, ellipse, or spline) over the organ of interest (i.e. liver, spleen, right/left kidneys) by using our developed Multi Planar Reconstruction (MPR) interface (Selver, Özdemir, & Selvi, 2013).

By this way, the approach in (Selver & Güzeliş, 2009) is further extended for abdominal organs by allowing the user to select an appropriate surface using our developed interface. Then, VHS is calculated on the user aligned axis (i.e. a slice plane with an arbitrary normal vector, not aligned with  $x$ ,  $y$ , or  $z$  axes).

It is observed that VHS can roughly differentiate the organ of interest even when it has an overlapping intensity range with other tissues. Albeit requiring a refinement step, the lobes of the VHS allow visualizing the organ of interest for an initial rendering by assigning color and opacity values to the selected lobes. With the help of this interactive process, VHS becomes an effective new domain as a search space for TF specification on abdominal MRI data.

The selection of the lobes from VHS requires an approximation to the data since VHS: i) is non-smooth due to MRI intensity fluctuations, ii) has varying intensity ranges for the same organ due to the acquisition parameters, and iii) has limited sampling along  $z$ -axis due to high inter-slice distances. To overcome these difficulties, a hierarchical approximation model is proposed. Using a multi-scale and oriented Gaussian basis, VHS is modeled up to a desired accuracy level. This is achieved by systematically decreasing the scale of the Gaussian functions through iterations. Then, the lobes, which correspond to the intensity range of the organ of interest, are used to determine a threshold range between certain lower and upper values. Finally, a fine classification is performed using morphological operations of erosion and dilation and region growing.

The rest of this thesis is organized as follows. Section 2 describes the MRI sequences and the datasets used in this study. Section 3 introduces the developed software and its graphical user interface (GUI), which can be interactively used to generate user aligned VHS. Section 4 describes the methodology in two steps. First, a coarse approximation to the user aligned VHS is performed by using a hierarchical multi-scale Gaussian approximation. Second, a finer classification is performed to the residual data by using spatial information. Section 5 presents the applications and the results. Finally, Section 6 includes the conclusions and the discussions.

## CHAPTER TWO

### MAGNETIC RESONANCE IMAGING AND MR DATASET

#### 2.1 Magnetic Resonance Imaging (MRI)

Radiologists utilize different types of medical imaging techniques to identify and remedy a particular disease or part of the body. The imaging techniques are chosen with respect to both the patient and the imaging method. The main goal of imaging systems, as related to the physics of their modality, is to produce accurate and useful images. To understand the key concepts, the following issues, should be considered (Prince & Links, 2006):

- i) Medical imaging relies on *noninvasive techniques* to image body structure and function.
- ii) Each technique or method is a different imaging modality.
- iii) The main imaging modalities are *projection radiography, computed tomography, nuclear medicine, ultrasound imaging, and magnetic resonance imaging*.
- iv) The signal of interest is defined by the modality and specific imaging parameters.
- v) Radiologists are trained to look for specific patterns, defined by the modality, specific imaging parameters, and differences in the expected signals between normal and abnormal (diseased) tissues.

MRI is an imaging technique that can generate high quality images of the interior of the body. MRI is based on the principles of nuclear magnetic resonance (NMR), a spectroscopic technique used by scientists to obtain microscopic chemical and physical information about molecules. In the beginning, MRI is defined as a tomographic imaging technique due to obtaining an image in a thin slice through the human body. Later, MRI has further moved into becoming a volumetric technique (Hornak, n.d.).

### ***2.1.1 What is an MRI Scan?***

MRI uses energy of magnetic field, radio wave pulses, and a computer to produce the images of organs and structures inside the body. The distinction of MRI is to provide different information about the structures of the body. It differs from other imaging systems such as X-ray, ultrasound, and CT scan. Images of an MRI scan can be visualized on a computer monitor and registered into a CD.

The MRI scanner is a unit which has a cylindrical shape surrounded by a circular magnet. The patient lies on a moveable examination bed that can slide into the magnet of the unit. The magnet creates a strong magnetic field that aligns the protons of hydrogen atoms, which are then exposed to a beam of radio waves. This spins the various protons of the body causing them to produce a faint signal that is detected by the receiver portion of the MRI scanner. The received information is processed by a computer and an image is produced. The magnetic field is produced by passing an electric current through wire coils in most MRI units. Figure 2.1 shows an MRI system with magnetic field lines (McRobbie, Moore, Graves, & Prince, 2003).

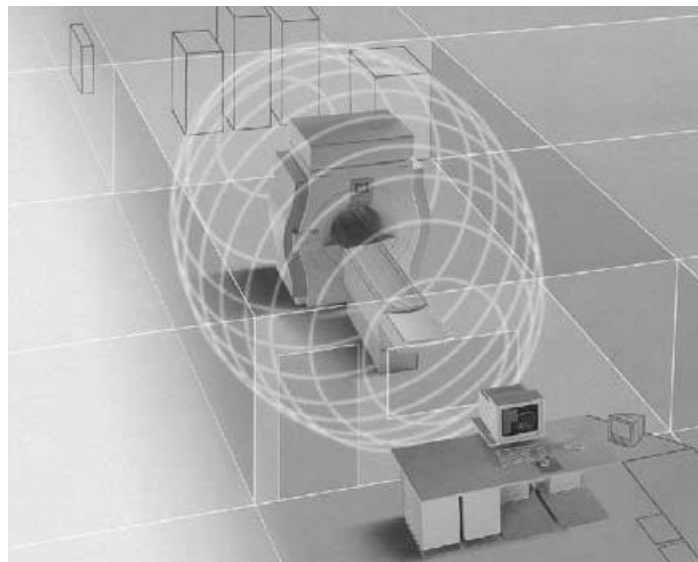


Figure 2.1 Extent of the 0.5 mTesla (mT) fringe field around a 1.5 Tesla (T); (Courtesy of Philips Medical Systems).

Other coils, located in the machine, and in some cases, placed around the part of the body being imaged, send and receive radio waves, producing signals that are detected by the coils. A computer then processes the signals and generates a series of images, each of which shows a thin slice of the body. The images can then be studied from different angles by an interpreting radiologist. Frequently, the differentiation of abnormal (diseased) tissue from normal tissues is better with MRI than with other imaging modalities such as X-ray, CT, and ultrasound (Magnetic Resonance Imaging (MRI) - Body, 2013).

## **2.2 MRI Sequences**

The tissues of the body can be classified roughly by considering their basic appearances:

- i. Fluids – cerebrospinal fluid (CSF), synovial fluid, oedema,
- ii. Water-based tissues – muscle, brain, cartilage, cardiac muscle,
- iii. Fat-based tissues – fat, bone marrow.

The variation of the tissues causes a variation in signal intensities. As a result, this variation affects the brightness and contrast of MR images. These differences allow us to realize the boundaries between tissues. As an example, if a tumor is bright and the brain has darker grey-levels, then the tumor can be detected easily. By adjusting the timing of the sequences and utilizing dissimilar imaging techniques, MR images can be obtained with a large range in terms of contrast. Having a lighter grey-level for tumor is not related with changing the look up table (LUT) which adjusts brightness or darkness. Tumor could have darker grey levels thanks to the MRI structure. Figure 2.2 shows a tumor in a human brain (McRobbie et al., 2003).

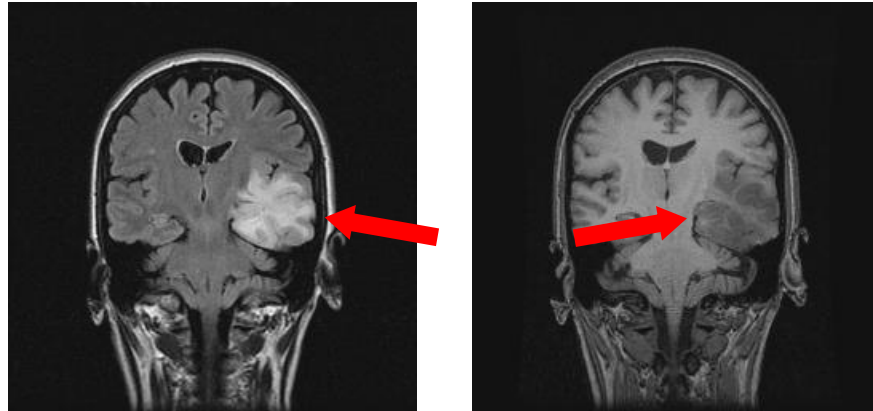


Figure 2.2 (a) Coronal image of the brain showing a tumor. In this image, the tumor is bright against the darker grey of the normal brain tissue. (b) The same slice with a different pulse sequence, this time showing the tumor darker than the surrounding brain tissue.

All MR images are produced using a pulse sequence, which is stored in the scanner computer. The sequence contains *radiofrequency (RF) pulses* and *gradient pulses* which have carefully controlled durations and timing (McRobbie et al., 2003). In addition to the importance of the radiofrequency and gradient pulses, the essential components for any imaging sequences are (Hoa, n.d.):

- i. An RF excitation pulse, required for the phenomenon of magnetic resonance.
- ii. Gradients for spatial encoding (2-D or 3-D), whose arrangement will determine how the frequency domain is filled.
- iii. A signal reading, combining one or a number of echo types (spin echo, gradient echo, Hahn echo, stimulated echo, etc.) determining the type of contrast.

Finally, the user must choose the following sequence parameters; Time of Repetition (shortly TR, the time between successive  $90^0$  pulses), Time of Echo (shortly TE, the time from the  $90^0$  pulse to the echo), flip angle, turbo factor, and field of view matrix to find the best compromise between contrast, spatial resolution, and speed.

### 2.2.1 MRI Sequences Process

MRI is based on natural magnetization that is induced in the human body when it is placed in the scanner. The strength of the magnetization depends on the *proton density* of the tissues. When a scanning sequence starts, the magnetization is knocked out of the alignment by one of the RF pulses and into the  $x - y$  or transverse plane. It creates a signal that can be manipulated by the rest of the gradient and RF pulses in the sequence. After the RF pulse, the magnetization goes back to its equilibrium position along the  $z$  plane. The relaxation of the RF pulses is seen in Figure 2.3 (McRobbie et al., 2003).

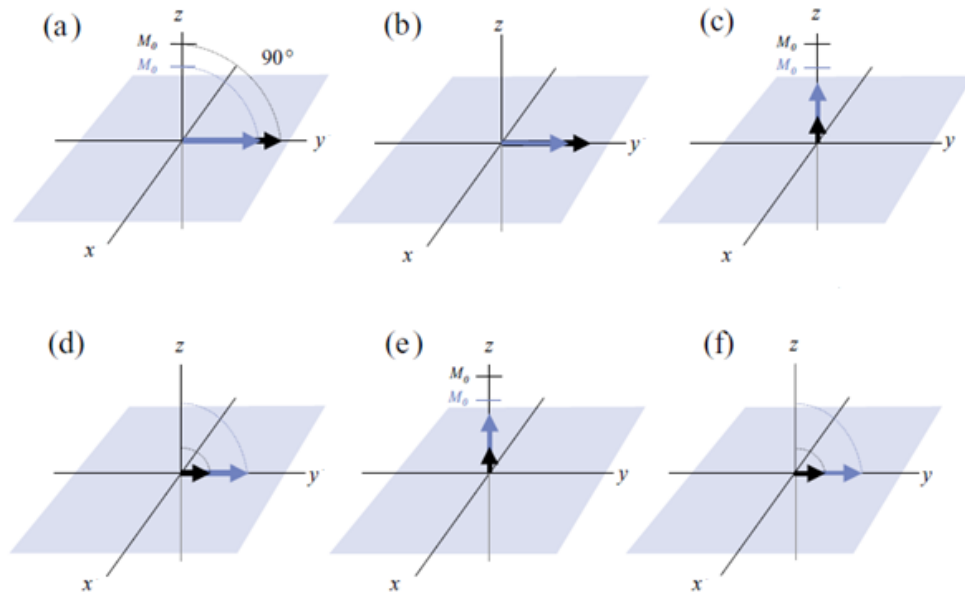


Figure 2.3 The basics of MRI (a) The tissues have different proton densities and  $90^\circ$  pulse is applied. (b) A  $90^\circ$  pulse knocks both magnetizations into the transverse plane where they create a signal. (c) After some time signal has decayed to zero while  $M_z$  recovers. (d) When the second  $90^\circ$  pulse is applied after time TR, reduced signals are rotated into the transverse plane. (e) After another TR, both  $M_z$  have recovered to the same height as before. (f) The third  $90^\circ$  pulse creates the same T1-weighted signal in the transverse plane.

### 2.2.2 Classification of MRI Sequences

There are two main sequence families, depending on the type of echo recorded. The *spin echo* is the most common sequence that is characterized by the presence of the type of  $180^\circ$  rephrasing RF pulse. The other one is the *gradient echo* which starts with a smaller RF pulse producing a flip angle (less than  $90^\circ$ ). Figure 2.4 illustrates the other sequences that belong to these two families (Hoa, n.d.).

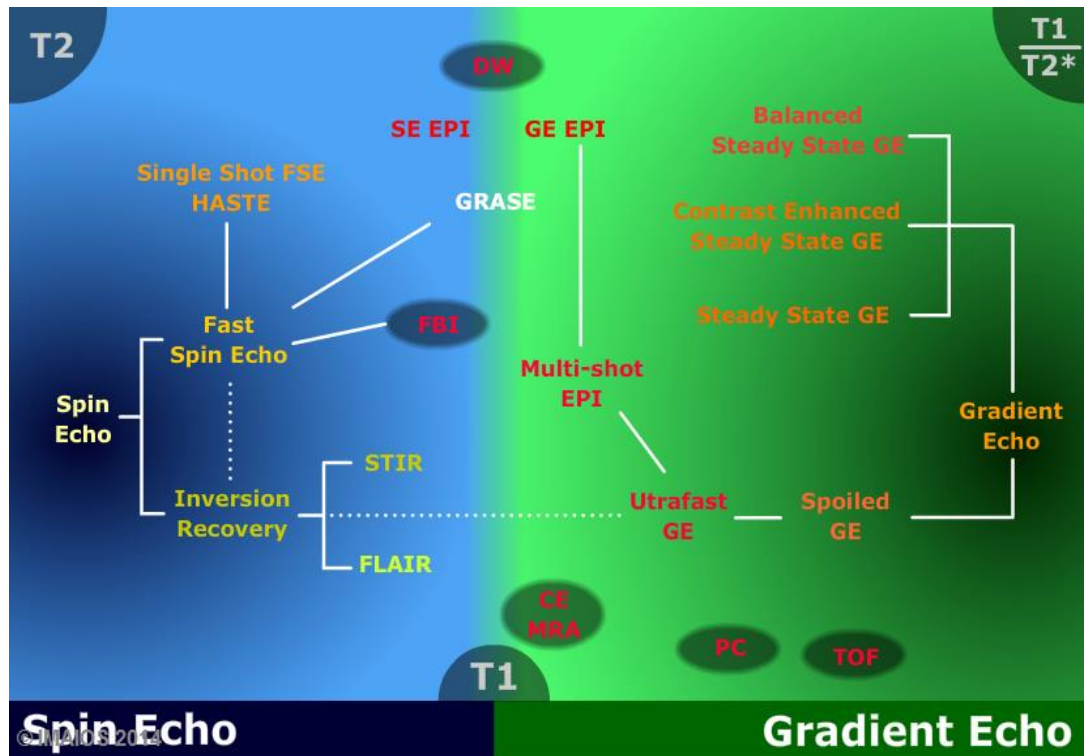


Figure 2.4 The classification of echoes.

The rest of this section introduces the MRI sequences (i.e. T2-SPIR, T1-DUAL, T1-WATS, and THRIVE) used in this study. Here, it is worth to point out that the names of the sequences are vendor dependent and in this thesis they are based on Philips abbreviations.

SPIR is the abbreviation for “Spectral Pre-saturation Inversion Recovery”. It is used as a hybrid imaging sequence. The SPIR sequence uses a T2-weighted contrast mechanism for imaging. It relies on selective suppression of fat protons (Westbrook



& Kaut, 1998). The pre-saturation pulse is applied separately to each slice selection gradient. This sequence requires sensitive adjustment of calibration and a very homogenous magnetic field. The above mentioned features of SPIR makes it a preferred sequence to study liver, because the liver parenchyma can be analyzed very well with suppression of the fat content inside the parenchyma. Especially, mass lesions belonging to parenchyma are more visible in this sequence. Due to being T2-weighted, it is possible to navigate the vessels within liver since they appear hyper-intense. The liver border appearance gets visually clearer, because of the suppression of the fat tissue around the liver. The adjacent abdominal organs and tissues such as gall bladder, duodenum contents, pancreas, and the right kidney become more separable from the liver with their high-valued signal intensity. One more important contribution of the SPIR sequence is its low sensitivity to patient or respiratory motions. This feature provides minimization of the artifacts that adversely affect image quality. Figure 2.5 shows some sample images in a T2-SPIR sequence.

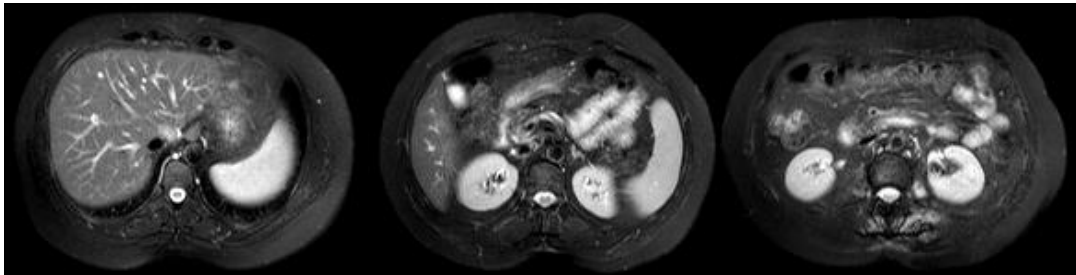


Figure 2.5 Different image slices of T2-SPIR sequence

T1-DUAL (in-phase and out-phase) is a fat suppression sequence, which uses the time differences in the z-axis recoveries of fat and water protons. The signal is acquired twice: first, when water and fat protons are in phase; and second, when they are out of phase (while excited protons are returning to their first position). For 1.5 T devices, the in-phase time, with water and fat protons in the same direction, is 4.6 ms and the out-phase time, with fat and water protons in the opposite directions, is 2.3 ms. By determining TE value with this information, fat suppression is accomplished by subtracting corresponding frequencies of fat and water signals. This sequence is very useful to understand the fat content in lesions. Since T1-DUAL is a T1-weighted sequence, it is very effective to identify blood and tissues that are rich in

protein. This sequence also helps in determining the level of liver lubrication. In out-phase images, the borders of the organs appear to be black, due to the sudden change in the amount of fat and water at the organ boundaries that cancel the acquired signal. This property of T1-DUAL is sometimes used for border delineation algorithms (Kellberg, Karlsson, Stokland, Svensson, & Dahlgren, 2010). Figure 2.6 shows some sample images in a T1-DUAL sequence.

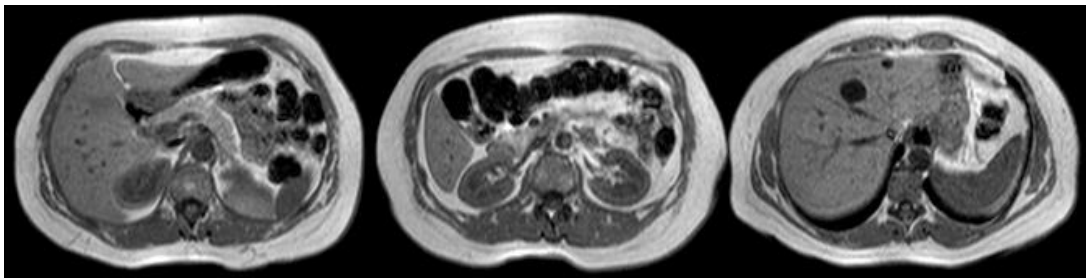


Figure 2.6 Different image slices of T1-DUAL sequence

SSH refers to single shot imaging. It is a quite useful sequence for the abdominal analysis, which is affected by the motion caused by vessels, intestinal gas, and diaphragm. By using this sequence, steady liquids can be studied very well, which allows analysis of biliary tracts. Figure 2.7 shows some sample images in an SSH sequence.

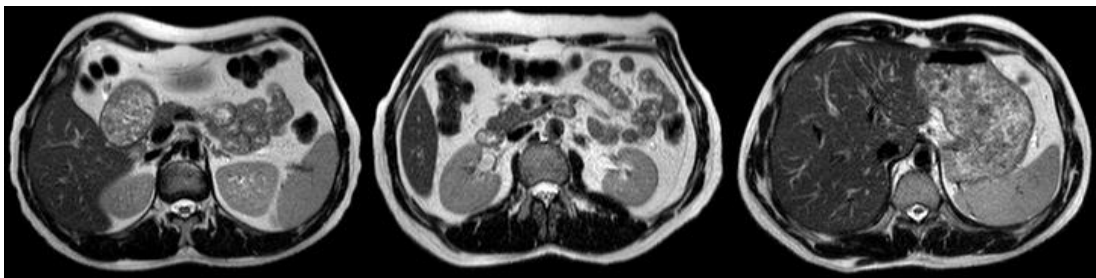


Figure 2.7 Different image slices of SSH sequence

THRIVE is a fast imaging sequence that is obtained by scanning the liver consecutively in a short time with thin slices to obtain the response of a known lesion to a contrast agent. THRIVE provides observation of the signal increase originating from the contrast agent instead of image quality. Figure 2.8 shows some sample images in a THRIVE sequence.



Figure 2.8 Different image slices of THRIVE sequence

### 2.3 Slice Thickness and Spacing

Slice thickness helps in obtaining high resolution and detailed images. By increasing the slice thickness, the energy of the noise decreases, but also the spatial resolution is reduced. Based on the changes in spatial resolution, the discernability of the tissues in the image series can be increased. This depends on a good coordination between slice thickness and spatial resolution. Slice thickness is one of the crucial factors for volumetric segmentation. Although it seems that small slice thickness is better for volume segmentation, it is known that this is not always the case (Hermoye, 2004).

Spacing or slice gap is the space between adjacent slices as measured in millimeters. It allows the technologist to control the size of the imaging volume by increasing and decreasing the space in between slices. Spacing provides a method to compensate for the imperfect radio frequency excitation pulse. Slice gap is the separation between two slices. It equals the difference between the slice thickness and slice interval (Westbrook, 2008).

### 2.4 Datasets

The analyses in this thesis work are applied to several MRI series, which are obtained at the Radiology Department of Dokuz Eylül University. The datasets are acquired using a 1,5 T Philips MRI modality that produces 12 bit DICOM images each of which has a resolution of 256 x 256. The datasets were retrospectively collected from the Picture Archiving and Communication System of the same

department. Five different MRI sequences (i.e. T1-DUAL (in-phase), T2-SPIR, THRIVE, T1-WATS, SSH) are used to test our proposed method. As described before, each of these sequences are used to scan the same part of the body. They are obtained from different combinations of radiofrequency pulses and gradients (Brown & Semelka, 1999; Westbrook, 2002).

In this study, 21 MRI datasets, which are obtained from 21 different patients, are used. The details about the characteristics of these datasets are given in Table 2.1. Four different sequences are acquired for each patient except one, who has 3 different sequences. While T2-SPIR, SSH, and T1-DUAL sequences are common for all 21 patients, 20 patients have either THRIVE (i.e. 7) or T1-WATS (i.e. 13) sequences. For T2-SPIR, which is common for all 21 patients, slice thickness value changes between 7.7 mm and 9 mm and has an average value of 8.6 mm. Moreover, the  $x$ - $y$  spacing in this sequence changes between 1.36 mm and 1.89 mm with an average of 1.53 mm. The number of slices for T2-SPIR sequence is 26 as minimum, 36 as maximum, and 30 as average. On the other hand, T1-DUAL sequences include two different series mentioned above. Each series has the same  $x$ - $y$  spacing, slice thickness, and number of slices. For T1-DUAL sequences, slice thickness has a value between 5.5 mm and 9 mm with an average of 7.84 mm. The  $x$ - $y$  spacing value in this sequence is between 1.44 mm and 1.89 mm with an average value of 1.61 mm. While the average number of slices is 32.8, the minimum number is 26 and the maximum number is 50. SSH sequence has a slice thickness between 5.5 mm and 9 mm with an average of 7.84 mm. For SSH sequences,  $x$ - $y$  spacing changes between 1.34 mm and 1.82 mm with an average of 1.56 mm. While average number of slices is 32.2, it is 50 at most and 25 at least. T1-WATS sequence, which is acquired for 13 patients, has a slice thickness value between 5.5 mm and 9 mm, just like T1-DUAL and SSH sequences, with an average of 7.9 mm. While  $x$ - $y$  spacing in T1-WATS sequences changes between 1.36 mm and 1.67 mm, the average value of  $x$ - $y$  spacing is 1.43 mm. Finally, THRIVE sequences, which only have 7 datasets, have differences compared to the other sequences. The slice thickness is smaller and does not change from patient to patient for THRIVE. All THRIVE series have 2.5 mm slice thickness. Since the slice thickness is smaller, THRIVE sequence has more

number of slices in one series. Number of slices is 110 at most and 80 at least. Average number of slices is 92.9. For THRIVE,  $x$ - $y$  spacing changes between 1.56 mm and 1.97 mm with an average of 1.67 mm. Table 2.1 gives the list of the datasets and the MRI sequences which are used in this study.

Table 2.1 The list of the datasets and the MRI sequences used in this study (mm).

MRI Seq.*	# of Datasets	Slice Thickness			x -y Spacing			# of Slices		
		Min	Max	Ave*	Min	Max	Ave	Min	Max	Ave
T2-SPIR	21	7.7	9	8.6	1.36	1.89	1.53	26	36	30
T1-DUAL	21	5.5	9	7.84	1.44	1.89	1.61	26	50	32.8
THRIVE	7	2.5	2.5	2.5	1.56	1.97	1.67	80	110	92.9
T1-WATS	13	5.5	9	7.9	1.36	1.67	1.43	26	40	30.6
SSH	21	5.5	9	8.1	1.34	1.82	1.56	25	50	32.2

Ave\* : Average

Seq.\* : Sequences

# CHAPTER THREE

## GENERATION OF ARBITRARILY ALIGNED VOLUME HISTOGRAM STACK (VHS)

### 3.1 Anatomical Planes

In the field of human medicine, it often proves necessary to refer to the body in universally recognized ways. Anatomical planes are part of these standards, and are represented by imaginary cuts to section off anatomical portions. There are a number of different anatomical planes, each giving a unique look at the human body. Figure 3.1 shows the planes of the human body. Figure 3.2 illustrates various images which are obtained from different anatomical planes.

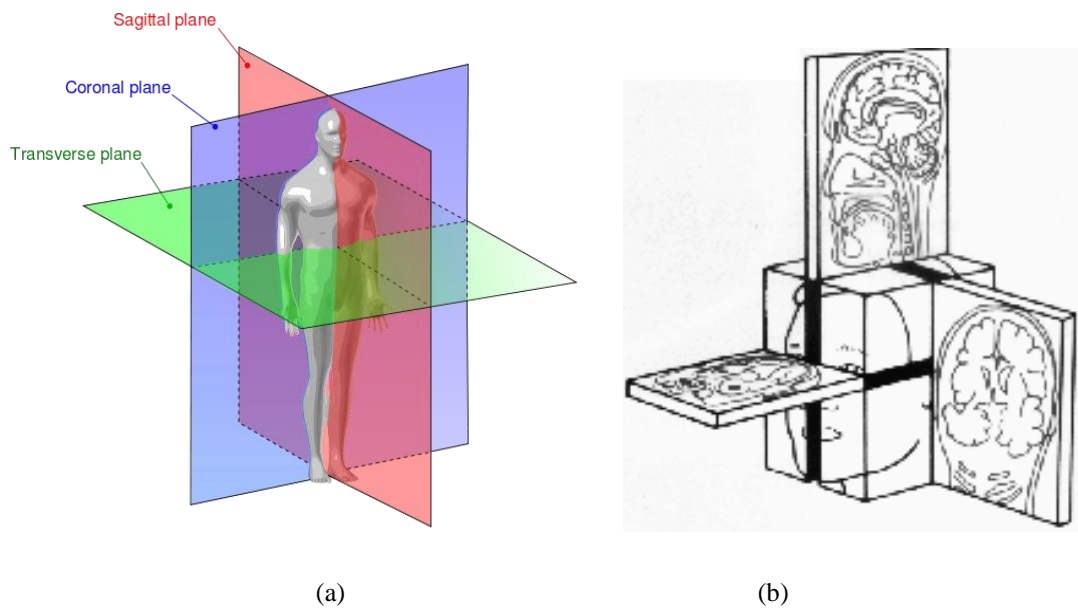


Figure 3.1 (a) Different anatomical planes of the human body, (b) imaging of different anatomical planes.

#### 3.1.1 Frontal (Coronal) Plane

One of the primary anatomical planes is known as the frontal plane. The frontal plane is represented by a vertical cut midway through the side of the body. To

visualize such a cut, one can imagine a vertical line passing through the middle of the side of the leg and continuing up and down the body. Using the frontal plane, doctors can separate the body into anterior or frontal, and posterior or rear portions. While this view provides a clear picture of the divide between front and rear, it gives no insight into the boundaries of the upper and lower portions of the body.

### ***3.1.2 Sagittal (Lateral) Plane***

The lateral plane divides the body in a familiar fashion. Also called the sagittal plane, the lateral plane is seen as a vertical cut through the center of the body. Rather than being parallel to the surface of the chest, as the frontal plane is, the sagittal plane lies perpendicular to the chest. This allows the lateral plane to divide the body into both left and right regions. Again, though it provides a different perspective than the frontal plane, the sagittal plane gives no reference to the vertical positions of anatomical portions.

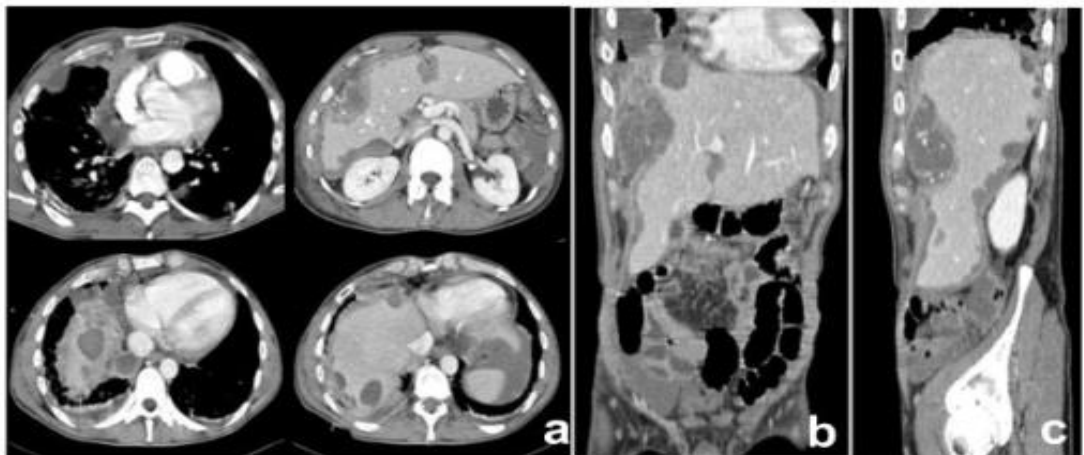


Figure 3.2 General overview of the different planes (a) axial, (b) coronal, and (c) sagittal plane.

### ***3.1.3 Transverse (Axial) Plane***

As mentioned previously, sagittal and frontal planes give no vertical reference points. Opposing these views of the body are transverse planes. Transverse planes are perpendicular to sagittal and frontal planes, representing horizontal cuts through

the body. The resulting upper and lower regions of the body can be useful for identifying the vertical positions of the relevant body parts. Of course, transverse cuts do not give consideration to horizontal positions, as sagittal and frontal cuts do. Figure 3.3 shows different slices from axial plane.

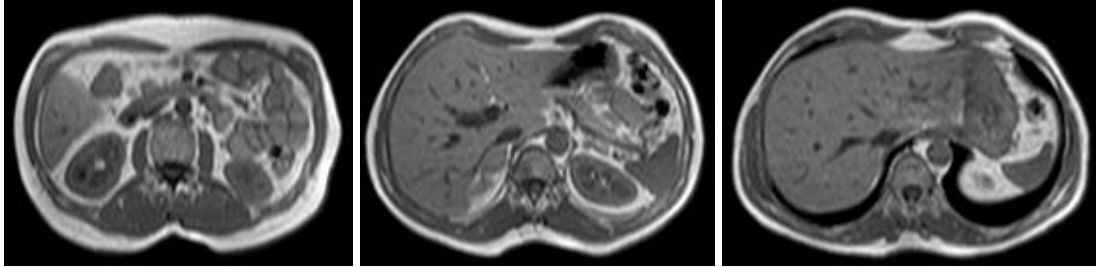


Figure 3.3 Different slices from axial plane

#### ***3.1.4 Oblique Planes***

Though the types of planes previously described are the most common in medical practice, they do not represent the only planes used. Essentially, any plane not falling into the category of sagittal, frontal, or transverse can be thought of as an oblique plane. Oblique planes, therefore, are the amalgamation of multiple plane types. As a result, oblique planes can often give the most accurate vertical and lateral positions of the body parts in question. It should be noted that oblique planes are not at right angles to the body.

As often as they are used in medical applications, anatomical planes prove their worth every day. Frontal planes provide views of the anterior and posterior portions of the body, while sagittal planes provide divisions between sides of the body. Using a horizontal cut, transverse planes divide the body into upper and lower portions. However, neither horizontal nor vertical cuts can fully describe the position of body parts, hence both are equally important. Oblique planes provide a compromise between both types of cuts, and with knowledge of all planes described above, anatomical positions can be accurately described as in Figure 3.4.



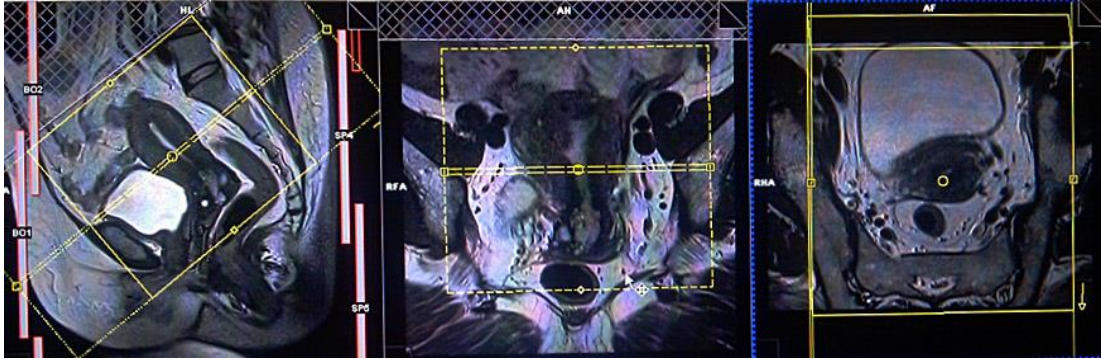


Figure 3.4 Oblique plane selection obtained from other planes

### 3.2 Developed Graphical User Interface (GUI)

Developed multi-planar reconstruction (MPR) software generates new reconstructed images using user inserted planes which are defined by the operator through a graphical user interface (GUI). The original pixel data from the series of slice images (original images) is assigned to a virtual voxel that is reconstructed according to the user inserted plane. The resulting images have the same slice thickness as the original image series. This provides a new volume of data that can represent the object of interest in a more focused way. To create the pixel values for the reconstructed image, volumetric information is used. When the dimensions of the scanned voxels (as set by slice thickness and in-plane resolution) are equal, the dataset is said to be isotropic. If the dimensions of the scanned voxel are not equal in all three planes, the dataset is said to be anisotropic. Isotropic data yields the best reconstructions.

In MRI data, using MPR images provides a wide perspective to the anatomy. They help in understanding and displaying tissues which are not well seen in the original images. MPR software typically uses an interactive GUI that allows the user to prescribe the reconstruction planes and parameters from simple reconstructed images, in a manner analogous to scanning the real patient. The user can select the orientation and thickness of the plane (typically equal or greater than the base scan thickness), and can indicate the number, location, and separation of reconstructed slices. Individual MPR programs have their own sets of rules and constraints for data

input, which can place limitations on the parameter choices in the original image series. Of greatest importance is the number of data points allowable (slices x number of rows x number of columns) which will, in the most part, be a function of computer memory. This limit is rarely reached, although it might be encountered in some sequence development applications.

The original scan data can be used to create images precisely aligned with anatomical planes and to create sets of slices with multiple orientations and slice thicknesses (at the same contrast weighting as the original scans). The MPR technique is an accessible tool that can replace or complement more conventional imaging approaches.

In MRI data, by using different anatomical reconstructions of various planes, MPR images provide a dynamic 3-D perspective of the organ of interest. Using a GUI for MPR imaging allows for the generation of multiple sequential sagittal and coronal images. Applying this reconstruction approach to MR abdomen images can shed light on a wide variety of pathological processes. The multi-planar MPR program can also expand the capacity of a radiologist to define a pathology.

In this thesis, this MPR approach is extended specifically for visualization of organs of abdomen (such as liver, spleen, right and left kidneys) by allowing the user to select a region by using an MPR GUI. In this thesis work, a new GUI is introduced. The aim of this GUI is to generate new images, which are re-generated based on the user inserted plane. This GUI supplies a new image series which is to be used together with a specialized algorithm.

### ***3.2.1 User Guide of the GUI***

The first step of the GUI is to upload 8-bit and 16-bit axial MR images which belong to the upper abdomen. The first address path in the GUI shows the subdirectories of the original 8-bit data which is uploaded by the user. The second address path indicates 16-bit (DICOM) data. The reason for uploading both 8-bit and

16-bit original data is going to be explained in the next section. The last address path constitutes the binary images of four organs, which could be either liver, spleen, right kidney, or left kidney, as labeled by radiologists. The binary address path is indicated by the region of interest. If the organ of interest is determined as the liver, then the binary images of the liver must be uploaded to the GUI. The “Browse” button is clicked on to upload the respective addresses. After selecting the addresses, the “Open” button loads the related images to the related axes of the GUI as seen in Figure 3.5.

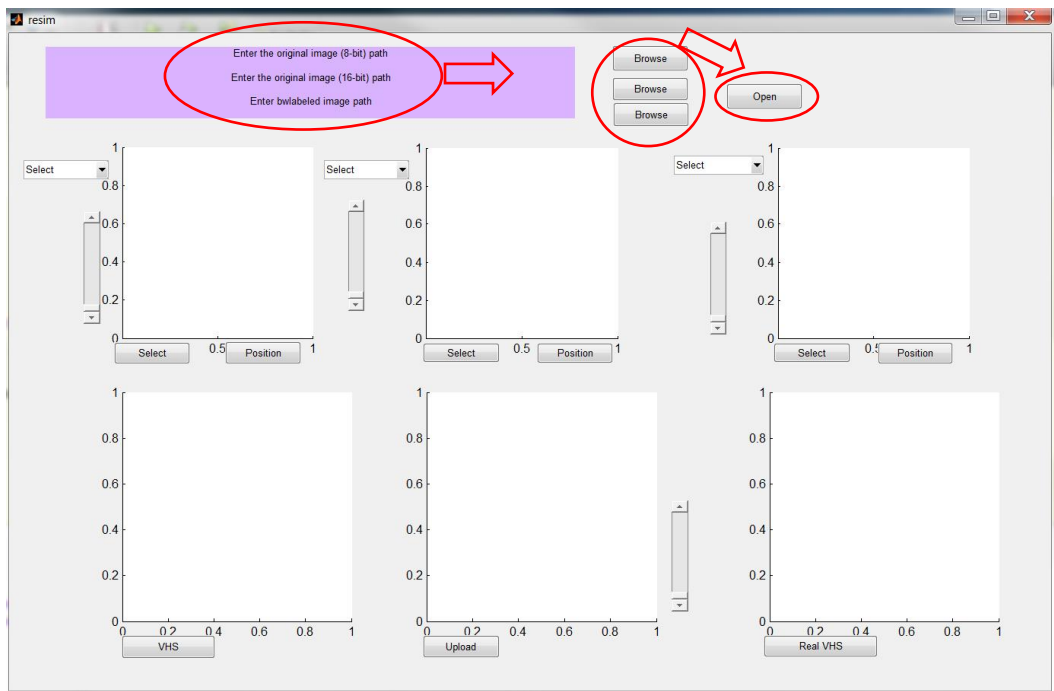


Figure 3.5 Address selection of the GUI

Instead of using coronal or sagittal images which are obtained from other GUIs, we generate our own sagittal and coronal images using our own GUI. In the construction of the sagittal and coronal images from other GUIs, some interpolation techniques are utilized. This can cause some losses in the original data.

The first plot displays the axial images that are uploaded by the user. MRI images have a resolution of 256 x 256. They constitute a part of the body with a series of 2-D images. These 2-D images are juxtaposed in the right order in order to construct a 3-D VHS in the form of a 3-D volumetric matrix. The first and second parameters of

the 3-D matrix are the width and height of the 2-D images, respectively. The third parameter of the matrix indicates the number of slices. If the number of slices is assigned as 25, then the size of the 3-D matrix becomes  $256 \times 256 \times 25$ .

The 3-D matrix is obtained by aligning the series in the right order. It can be easily obtained by using different images which belong to different planes. The important point is to change the matrix plane in the correct way. The coronal plane visualizes a cut as one can imagine a vertical line passing through the middle of the side of the leg and continuing up and down the body. This plane gives a frontal visualization of the organ of interest. In generating a coronal image, the first parameter becomes the number of slices and the other parameters constitute the size of the coronal image. Then, the size of the coronal image becomes  $256 \times 25$ . The coronal image is displayed in the GUI in the second plot.

The third and last plane is the sagittal plane that cuts vertically through the center of the body. It allows a lateral plane to divide the body into both left and right regions. The second parameter of the 3-D matrix indicates the number of slices. The size of the sagittal images is  $256 \times 25$ . Axial, coronal, and sagittal plane images are shown together in Figure 3.6.

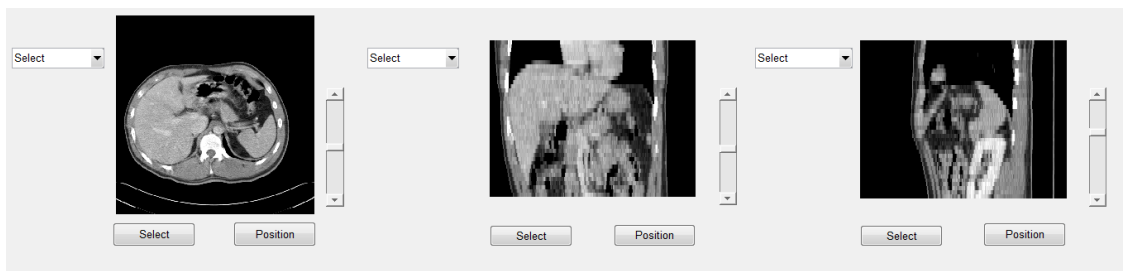


Figure 3.6 Axial, coronal, and sagittal plane images of the GUI

The sizes of the coronal and sagittal images are incompatible because of the difference in the width and height of images. To overcome this incompatibility, linear interpolation is applied to these images. We would like to stress that this interpolation is only used for the purpose of visualization. During processing,

original sizes are used to avoid any loss of original data. Each plot has its own sliders and by scrolling the sliders up and down individually, different slices are visualized. Each plot has its own pop-up menu on its left side and has its own “Select” and “Position” buttons at the bottom as seen in Figure 3.5.

The interaction mechanism enables the user to select an elliptical, a rectangular, or an arbitrary surface in any one of the three MPR constructions (i.e. axial, sagittal, and coronal planes). The area, which is selected by the user, is defined as the Region of Interest (ROI). The selection of the area should be consistent with the shape of the organ to be visualized. As an example, it can be stated that the geometrical structure of the kidney is circular. Therefore, applying a circular surface is more efficient than utilizing any other surface. As a second example, selecting a rectangular surface to construct MPR from liver is not logical. The main reason for this is the incompatible structure of the liver because liver is one of the largest organs in the abdominal region. Drawing a rectangle on the liver, which covers the liver at all slices, requires a rather large rectangular area. This means that instead of using a rectangular surface for the construction of liver, the information present on the left side of the body for the liver can be used.

By using this information in the selection of the cross section, an elliptical or a rectangular surface for kidneys is appropriate. Spline is suitable as a surface for large organs such as liver and spleen. The selection of the cross section constructs the width of the MPR image by using different methods. The height of the MPR image is defined by the user between the two left planes which are not selected during surface determination. Each pop-up menu includes line, ellipse, rectangle, and spline selections.

I) Selecting a line for MPR construction:

This step determines the height of the MPR image by using the “*imline*” command of the Image Processing Toolbox of MATLAB. The selection of the surface plane defines how the line must be used (vertical or horizontal) in other planes. The height orientation is shown in Figure 3.7.

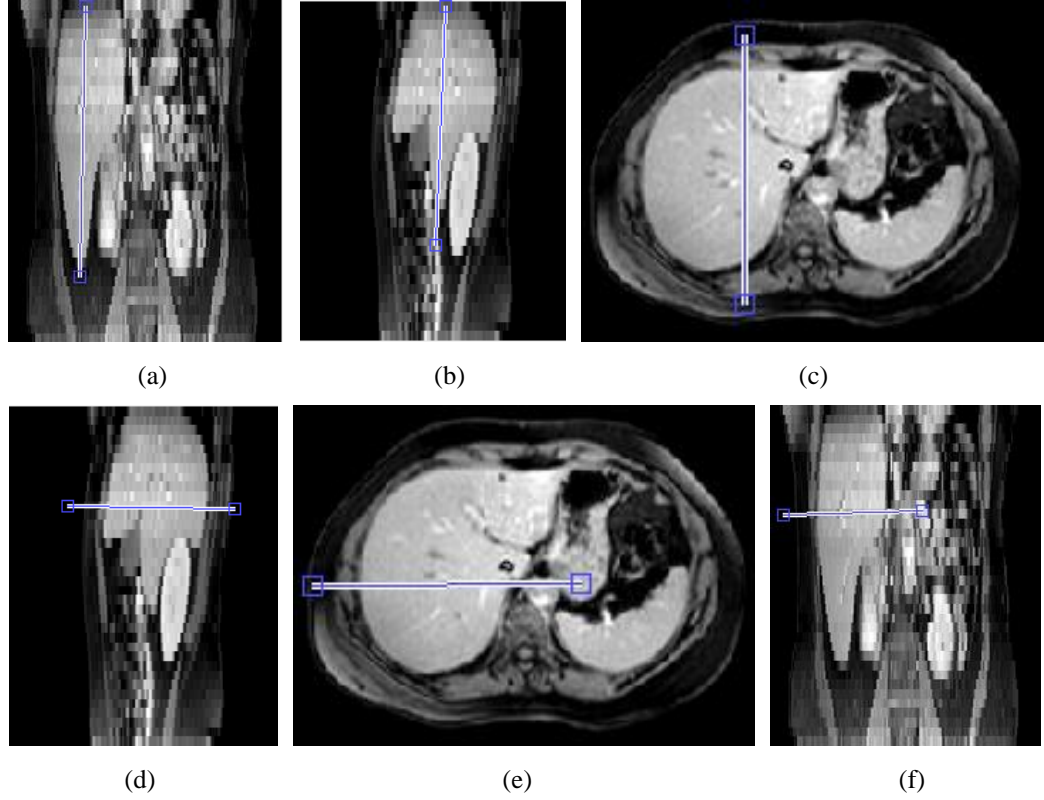


Figure 3.7 Line selection with respect to selected surface plane. Surface selection is from axial plane. Line selection is in (a) coronal plane and (b) sagittal plane. Surface selection is from coronal plane. Line selection is in (c) axial plane and (d) sagittal plane. Surface selection is from sagittal plane. Line selection is in (e) axial plane and (f) coronal plane.

## II) Selecting an elliptical surface for MPR construction:

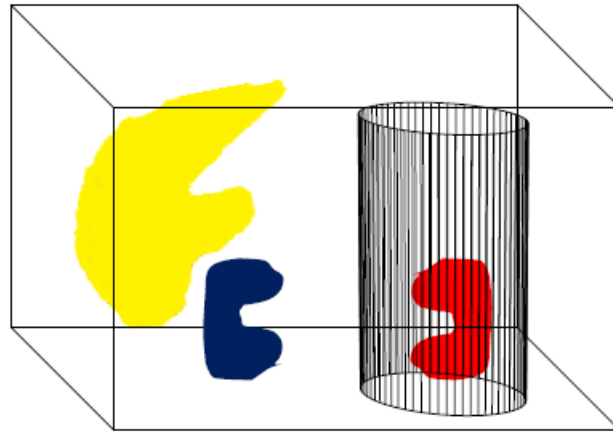
This step determines the center and radius of the 3-D elliptical cylinder. The cylinder formula is given as

$$\frac{x^2}{a^2} + \frac{y^2}{b^2} = 1 \quad (3.1)$$

where  $x$  and  $y$  are the coordinates of any point on the ellipse and  $a$  and  $b$  are the radii along the  $x$  and  $y$  axes, respectively.

2-D images are combined as a 3-D matrix and MPR images are obtained according to the drawn ellipse. To provide unity in terms of the sizes of the new images, long radius of the ellipse is chosen. The long radius indicates the width of

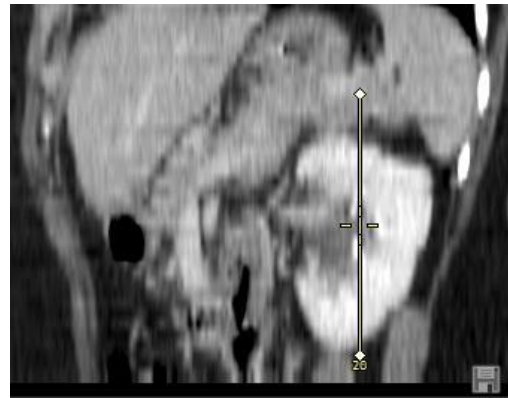
the new images. Then, using an MPR image, which is orthogonal to the MPR image used in the first step, the height of the cylinder is determined. Based on a defined thickness, new image slices, all of which have the same center position and size of (2 x long radius x height), are generated. The angle resolution is defined as  $10^0$ . Figure 3.8 shows the construction of MPR image and Figure 3.9 shows ellipse selections in all planes.



(a)



(b)



(c)

Figure 3.8 (a) Reconstruction strategy inside the volume, (b) circular area selection from axial, (c) vertical height selection from sagittal (left kidney)

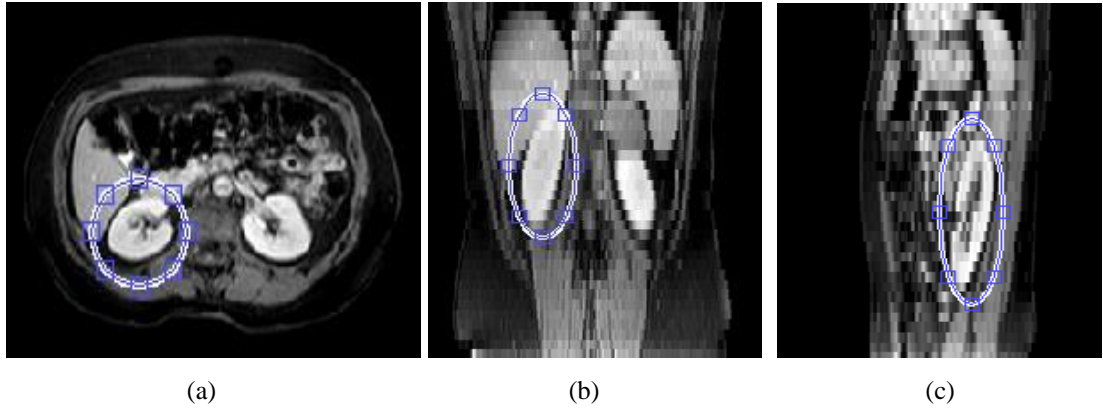


Figure 3.9 Ellipse area selection from (a) axial, (b) coronal, and (c) sagittal plane

### III) Selecting a rectangular surface for MPR construction:

This step is similar to the ellipse selection. The only difference is to define a surface which is rectangular. This creates a 3-D rectangular prism instead of a 3-D cylinder. Then, using an MPR image, which is orthogonal to the MPR image used in the first step, the height of the prism is determined. To have compatibility in the construction, new image slices must be in the same size. Therefore, as a width parameter, the longer side of the rectangle is chosen. Finally, based on a defined thickness, new image slices, all of which have the same center position and size of (2 x longer side x height), are generated. The angle resolution is defined as  $10^0$ . Figure 3.10 shows the construction of MPR image and Figure 3.11 shows rectangle selections in all planes.

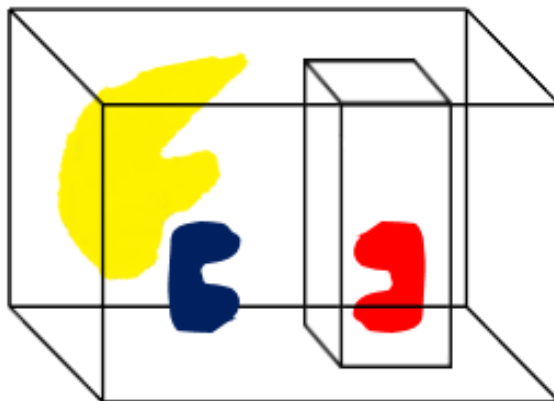


Figure 3.10 Reconstruction strategy inside the volume for rectangular area



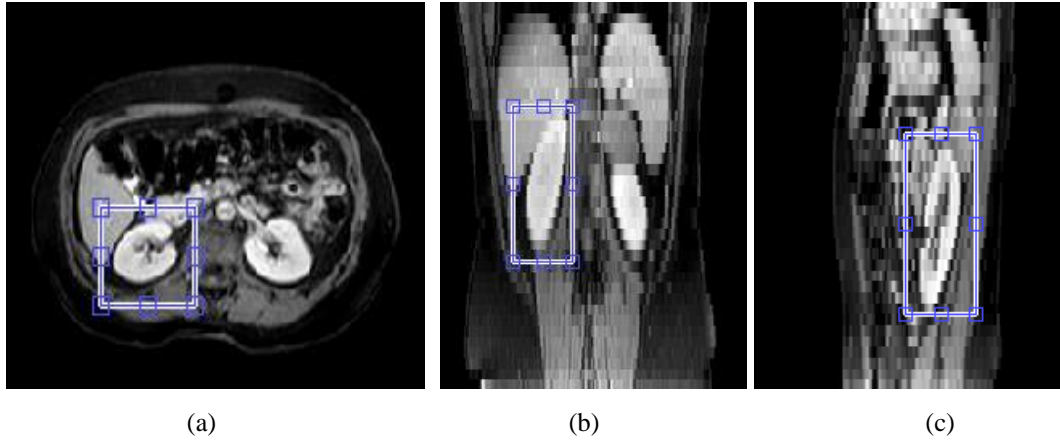


Figure 3.11 Rectangular area selection from (a) axial, (b) coronal, and (c) sagittal plane

#### IV) Selecting an arbitrary surface by drawing a spline:

Spline algorithm is different from the other surface options. It is based on the “*imfreehand*” command of the Image Processing Toolbox of MATLAB. “*imfreehand*” starts the process of interactive placement of an arbitrary region of interest on the current plots. A freehand region of interest can be dragged interactively using the mouse and supports a context menu that controls aspects of its appearance and behavior. The first and last points of the spline must contain the pixels of the organ of interest in all images where the organ exists. The first and last points are known and spline is divided into certain intervals. The stepping of this interval is defined automatically. After drawing the spline, certain lines are created by the algorithm such that the midpoints of these lines pass through the specified points. These lines are perpendicular to the spline and all of them has the same default length as 100. The length of the lines is adjustable and can be controlled by the user. Figure 3.12 shows spline selections in all planes and Figure 3.13 shows MPR images with respect to all planes.

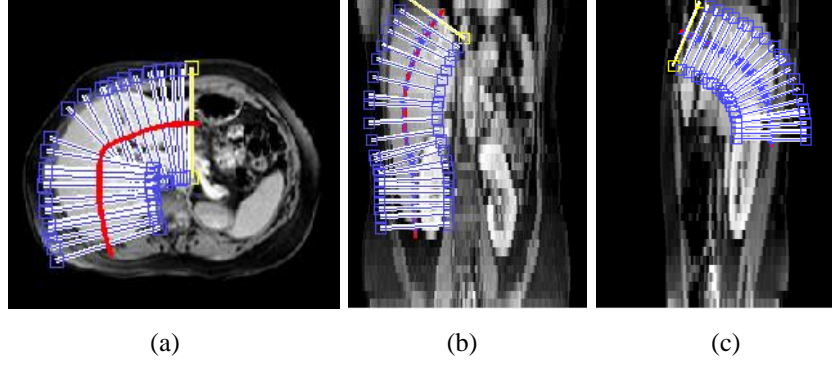


Figure 3.12 Spline selection on liver (a) axial plane, (b) coronal plane, (c) sagittal planes.

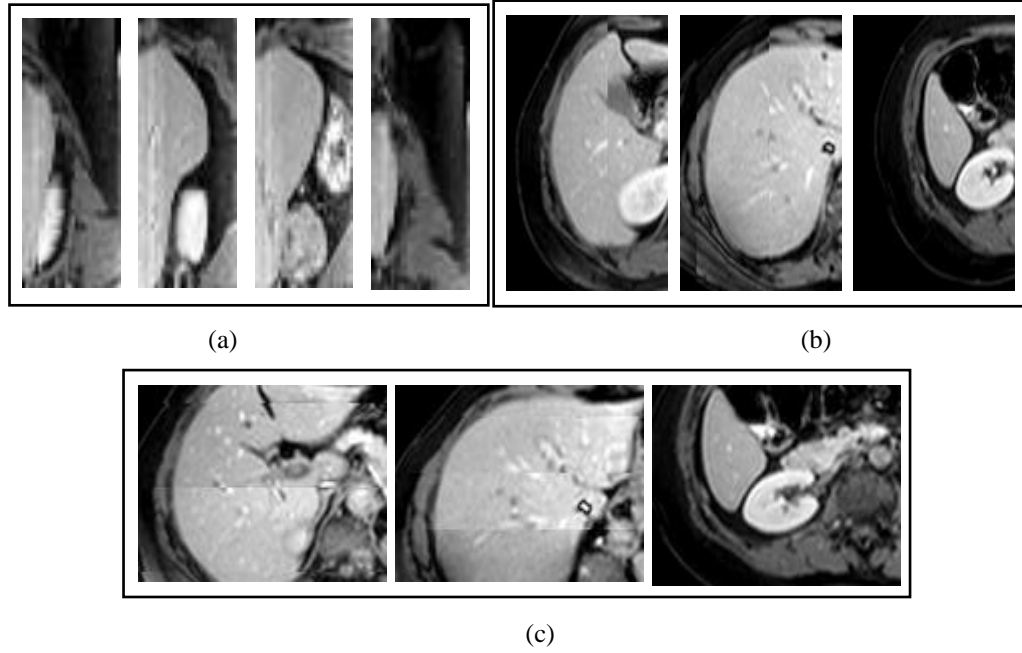


Figure 3.13 MPR images which are obtained from (a) axial, (b) coronal, and (c) sagittal planes

### 3.3 Computation of VHS

In CT datasets, the organs in the abdomen may have different gray value distributions due to environmental circumstances, injection of a contrast media, and certain modality parameters. Moreover, their location, orientation, and size may differ based on patient anatomy. Figure 3.14, Figure 3.15, and Figure 3.16 illustrate the gray levels and shape variations in abdominal organs. Although, there is a calibrated intensity scale in CT (i.e. Hounsfield Units – HU), the above mentioned diversity still exists. Moreover, volume rendering is not commonly used for MR datasets since there is no calibrated intensity scale. An MR dataset does not have a specific gray level range in contrast to a CT dataset, because MRI can easily be

affected by imaging artifacts. Many artifacts have a characteristic appearance and, with experience, they can be readily identified: MR hardware and room shielding, MR software, patient and physiologic motion, tissue heterogeneity, foreign bodies, Fourier transform and sampling (Gibbs artifact, zero-fill artifact, and aliasing artifact which occurs in the frequency domain).

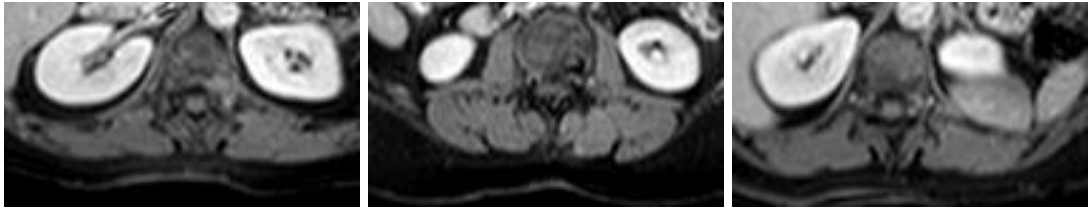


Figure 3.14 Gray levels and shape variations in the kidneys

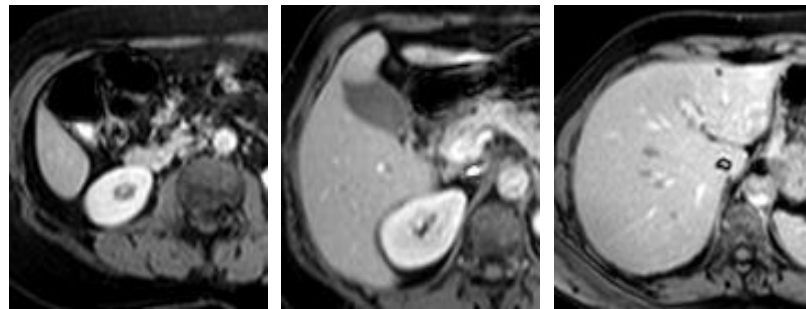


Figure 3.15 Gray levels and shape variations in the liver

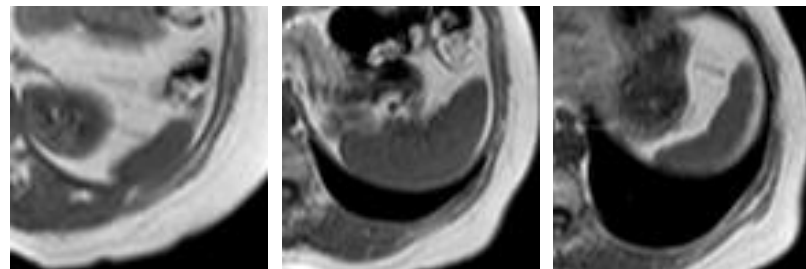


Figure 3.16 Gray levels and shape variations in the spleen

In the conventional approach, for both CT and MR datasets, the volume histogram is the main guide to find the tissues of interest. The characterization of the tissues would not be a crucial task if the tissues matched almost exactly with the visible peaks. Unfortunately this is not always the case. The peaks, which belong to the tissues, might be suppressed by more pronounced peaks of insignificant tissues. Especially in abdominal MR datasets, soft tissues and organs (i.e., liver, kidney,

spleen, aorta, muscle tissue, etc.) exist in a very narrow range of gray values. This makes working with MR datasets difficult in such regions as abdomen which is complicated. Besides, it renders the usage of the TF quite difficult for visualizing abdominal organs.

Medical datasets are formed by slices of the region of interest of the body. Thus, the typical appearance of an abdominal organ starts as a small object. By going forward through the slices, the organ appears larger. Around the middle of the image series, the organ of interest assumes its largest size. Then, the organ starts to look smaller again and slowly disappears in the continuing slices. It can be clearly stated that in the middle of the image series organs appear larger. At the beginning and end of the slices, organs look rather smaller. This causes a lobe-like histogram distribution for a tissue/organ which has usually a shape similar to a radially asymmetric (elliptical) Gaussian. The effect of having a lobe-like distribution is visible for most studies and cases, although not always. The four abdominal organs (liver, both kidneys, and spleen) successively appear and disappear in the image series. Also, they are large enough so that they can appear significantly in the dataset. This information can be exploited by using the  $z$ -dimension (orthogonal to the slices). Organs that are spatially separated in the  $z$ -dimension produce separate lobes. However, they produce intersecting lobes if they are spatially non-separated.

VHS is recently introduced in (Selver & Güzeliş, 2009) as a new domain which is created by aligning the histograms of the image slices of a CT/MR series. To generate a VHS, first, the histograms of the images in the dataset are calculated individually. Second, each histogram is aligned in the same order with images (i.e. from the first to the last). Ordering the histograms on the  $y$ -axis, which defines the number of slices, provides a 2-D histogram (i.e. VHS). In VHS,  $x$  axis represents the gray levels,  $y$  axis represents the number of slices, and  $z$  axis shows the number of pixels.

Our GUI, which is introduced in the previous section, provides a new image series by using different anatomical planes. Our main goal in the GUI is to take

advantage of the visualization of the organ of interest in the right way. Traditional volume histograms include a lot of information which causes serious segmentation problems. Dealing with abdominal region and difficulties of MRI make the segmentation of the organ of interest challenging. The difficulty is caused by the similarity of the gray levels of the adjacent tissues and the complex structure of the abdominal region. Therefore, instead of the aligning the axial, coronal, or sagittal slice histograms, we align the histograms of the new images. Thanks to its desirable properties, VHS incorporates spatial domain knowledge with local distributions of the tissues and their intensities. Figure 3.17 shows the construction of a VHS.

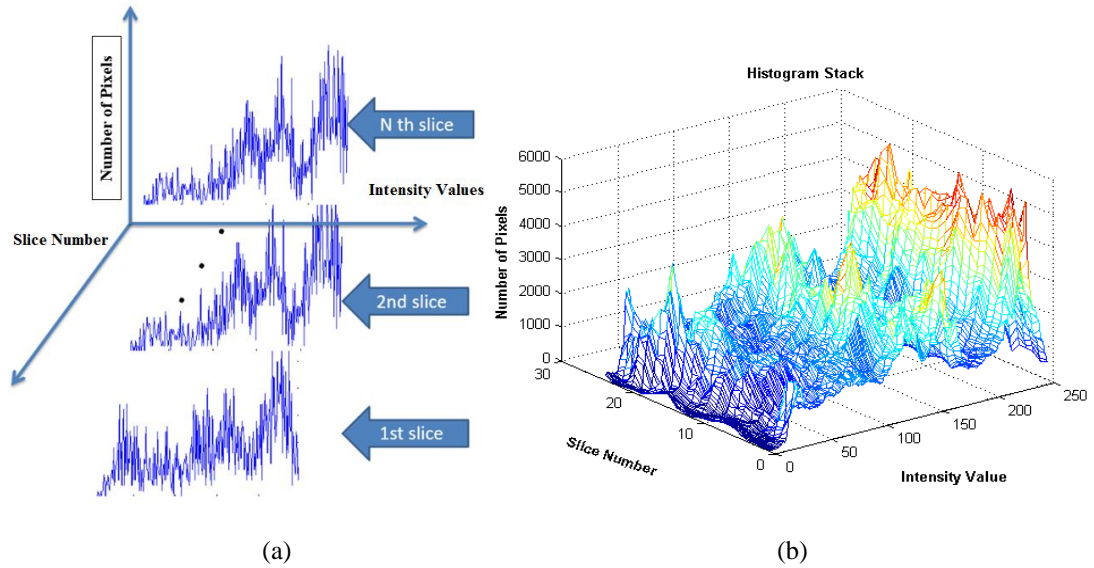


Figure 3.17 (a) Aligning the histograms of the image slices of an MR series, (b) an example of VHS.

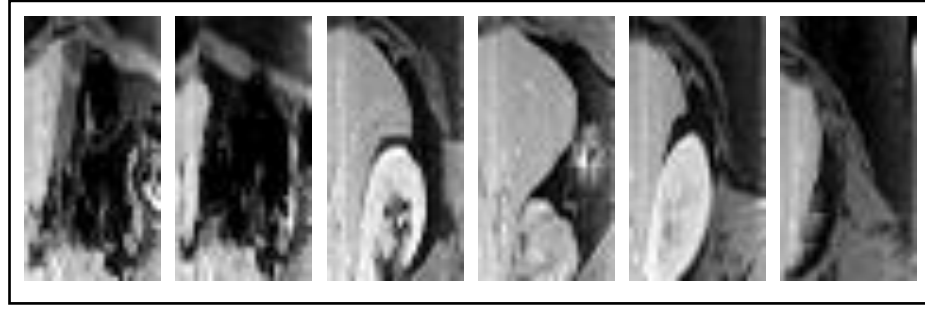
The VHS data presents more information thanks to the usage of all slice histograms separately. Using all slice histograms creates an inter-slice spatial domain. This new domain demonstrates changes in the gray level values through the series of slices, thus includes information on local histogram distributions of the tissues of interest. The variability of the gray level is much more distinguishable than a volume histogram. The main reason for this diversity is exploitation of spatial information. The tissues which are at different slices but with similar gray level distributions can clearly be distinguished by using this spatial information.

In this thesis, to improve the lobe like shape of an abdominal organ of interest, VHS is not calculated directly by MRI acquired image slices. Instead, a GUI is designed to provide a simple but effective interaction.

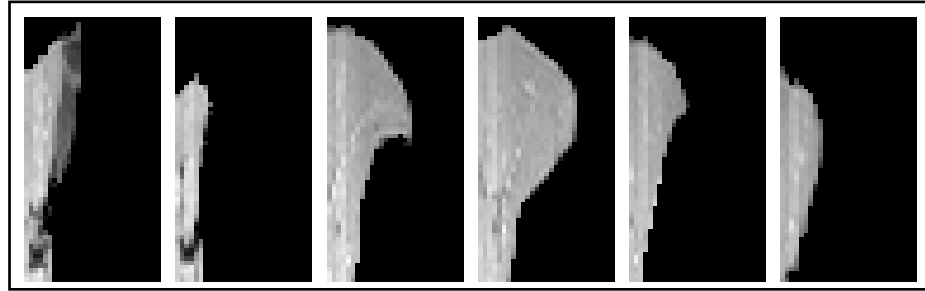
### ***3.3.1 The Interaction between the GUI and VHS***

In Section 3.2, the construction of the MPR is expressed in detail. However, using the GUI is more beneficial for the segmentation process. Our main goal is to ease the segmentation of the tissue of interest from VHS. In this section, VHS tool of the GUI is introduced.

After indicating the parameters of MPR, new slices are obtained automatically. By clicking on “VHS” button, new images are constructed and saved in a folder which is in the same directory with MATLAB. After the registration process, VHS is obtained by using the new slices. It is already mentioned that the third address path belongs to the binary image labeled by radiologists. The purpose of using these images is to measure the accuracy of the algorithm. Binary images are composed of zeros and ones which represent the background and the organ of interest, respectively. To obtain a benchmark data, new slices are constructed with the help of the binary images. These new slices are constructed as MPR images with the difference that the background of these images are composed of zeros. Therefore, the VHS of these images forms the benchmark histogram for the algorithm since the unwanted components are eliminated by replacing the appropriate pixels with zeros. Figure 3.18 shows the MPR images and the new slices which generate the benchmark data. By clicking on “Real VHS” button, benchmark data is constructed by using the new slices. These slices are saved in a folder just as MPR is.



(a)



(b)

Figure 3.18 (a) MPR images obtained from the GUI, (b) the benchmark data of the reconstructed images

Figures 3.19 and 3.20 illustrate the GUI such that ellipse is selected from the axial plane and the height is selected from the coronal plane. Side and top views of the VHS are also seen. Figure 3.21 and 3.22 show that spline is selected from the axial plane and the height is selected from the coronal plane.

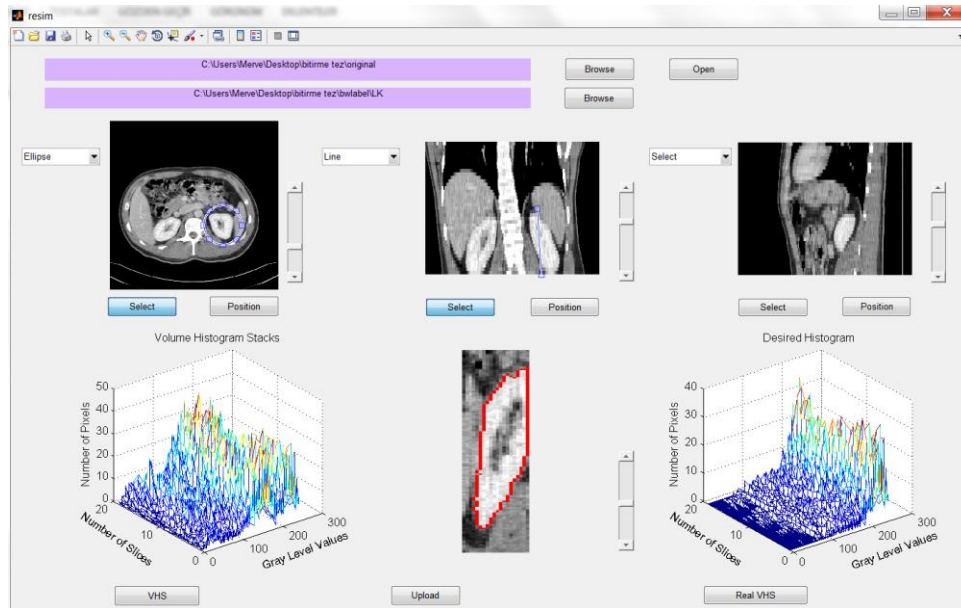


Figure 3.19 Ellipse is selected from the axial plane and the height is selected from the coronal plane

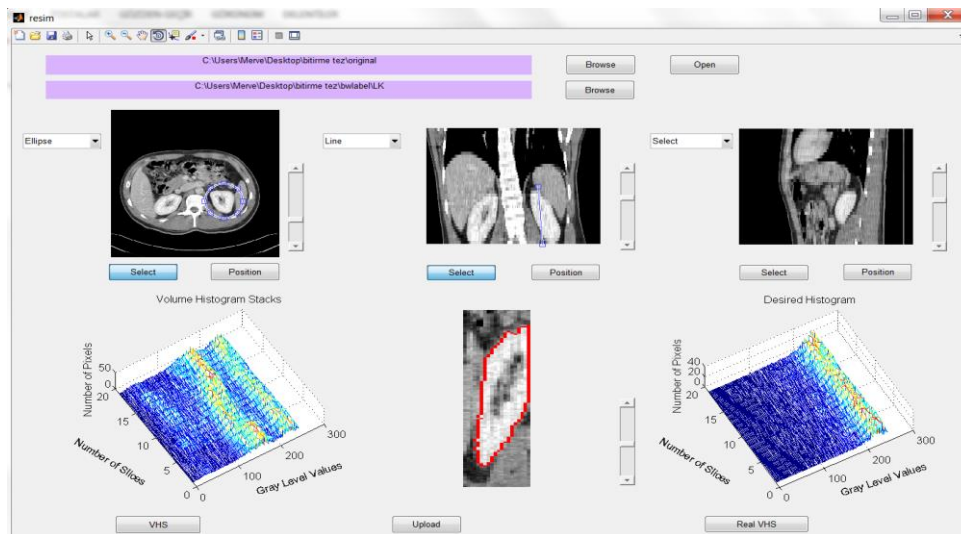


Figure 3.20 Ellipse is selected from the axial plane and the height is selected from the coronal plane with a different VHS view

In the second row, the middle plot shows the new MPR images. The axial images are labeled by the radiologist. During the construction of the MPR image, the newly labeled images are generated and the boundary of the organ of interest is drawn with a red label. The button “Upload” sets newly labeled images. By scrolling sliders on the right, newly labeled images are displayed easily.



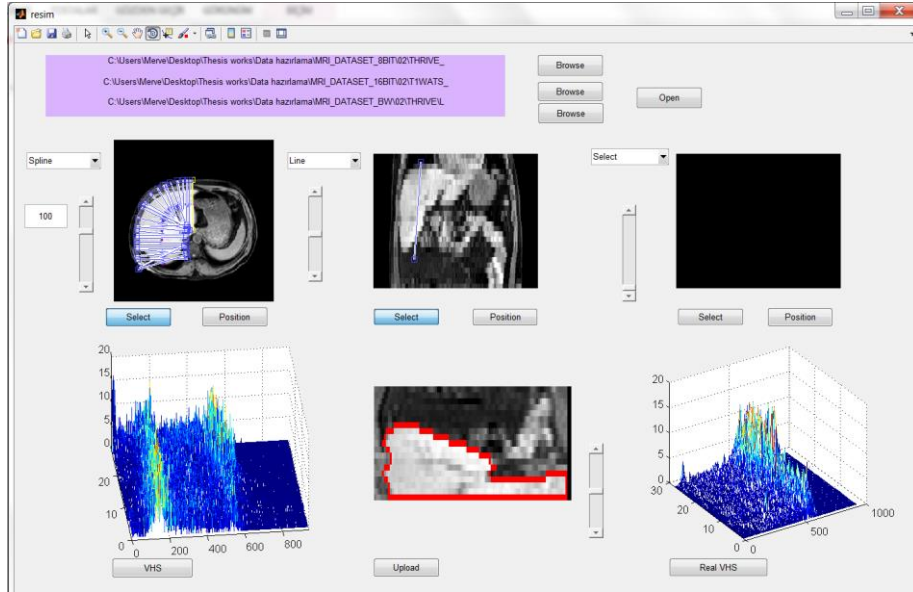


Figure 3.21 Spline is selected from the axial plane and the height is selected from the coronal plane

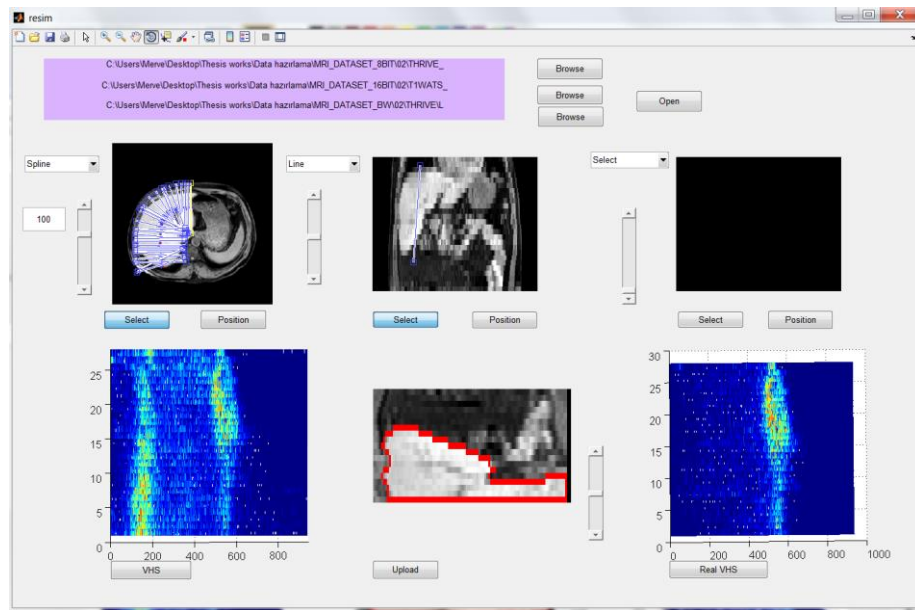


Figure 3.22 Spline is selected from the axial plane and the height is selected from the coronal plane with a different VHS view

Such an approach enhances the histogram and increases the differentiability of the organ of interest via a thresholding operation. The threshold values can be determined by finding the valleys on the right and left sides of the lobe of interest. As seen in Figure 3.23, our desired VHS has a rotated and scaled Gaussian structure. It

can also be said, by considering the original data, that there is a valley between the desired histogram and the unwanted components.

Here, it should be noted that the gray value ranges for organs of interest have varying intensity values and characteristics even for the same organ in different MRI acquisitions. Therefore, a method should be developed to model the VHS and determine the two valleys so that upper and lower thresholds can be assigned correctly. We use DICOM image series, in order to supply large numbers of gray levels, which is necessary to obtain a compact desired histogram.

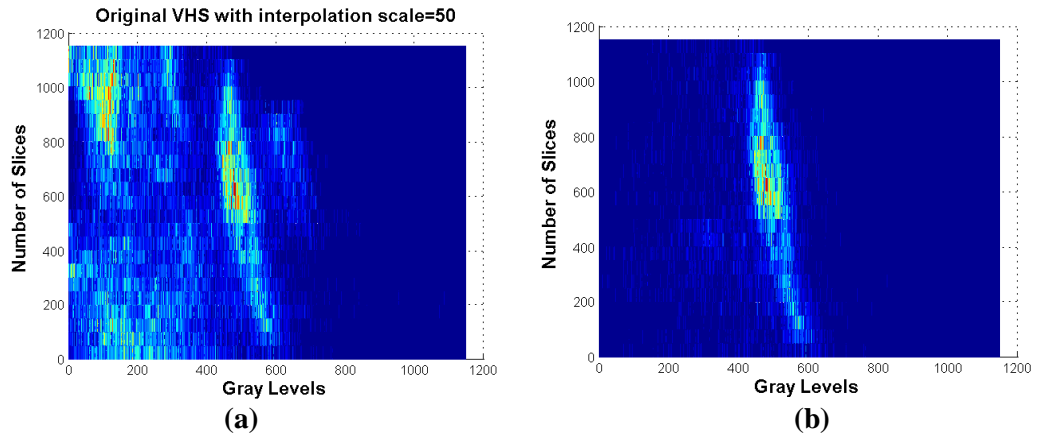


Figure 3.23 (a) VHS of MPR images which are obtained via splines, (b) desired histogram of the obtained MPR

## CHAPTER FOUR

### GAUSSIAN APPROXIMATION MODEL

#### 4.1 Gaussian Function

In scale space representations, Gaussian functions are used as smoothing kernels for generating multi-scale representations in computer vision (Chan & Vese, 2002) and image processing (Wink & Roerdink, 2004). Specifically, derivatives of Gaussians are used as a basis for defining various types of visual operations. Gaussian functions are also used to define certain types of artificial neural networks (Jain, Jianchang, & Mohiuddin, 1996). In signal processing, they serve to define Gaussian filters, such as in image processing where 2-D Gaussians are used for Gaussian blurs (Irani & Peleg, 1991). In digital signal processing, one uses a discrete Gaussian kernel which may be defined by sampling a continuous-time Gaussian function.

A one-dimensional Gaussian function is a curve of the form

$$f(x) = Ae^{-\frac{(x-\mu_x)^2}{2\sigma_x^2}} \quad (4.1)$$

where the parameter  $A$  represents the amplitude,  $\mu_x$  is the position of the center of the peak, and  $\sigma_x$  controls the width of the curve.

In two dimensions, one can vary a Gaussian using more parameters. Not only may one vary a single width, but two separate widths. We can also rotate a 2-D Gaussian function. Thus, we can obtain both circular Gaussians and elliptical Gaussians, depending on the support regions which are either circles or ellipses. A particular example of a 2-D Gaussian function is defined as

$$f(x, y) = Ae^{-\left[\frac{(x-\mu_x)^2}{2\sigma_x^2} + \frac{(y-\mu_y)^2}{2\sigma_y^2}\right]} \quad (4.2)$$

where the coefficient  $A$  is the amplitude,  $\mu_x$  and  $\mu_y$  are the centers, and  $\sigma_x$  and  $\sigma_y$  are the widths with respect to  $x$  and  $y$  axes, respectively. Figure 4.1 shows a 2-D Gaussian function with parameter values,  $A = 1$ ,  $\mu_x = 0$ ,  $\mu_y = 0$ ,  $\sigma_x = \sigma_y = 1$ .

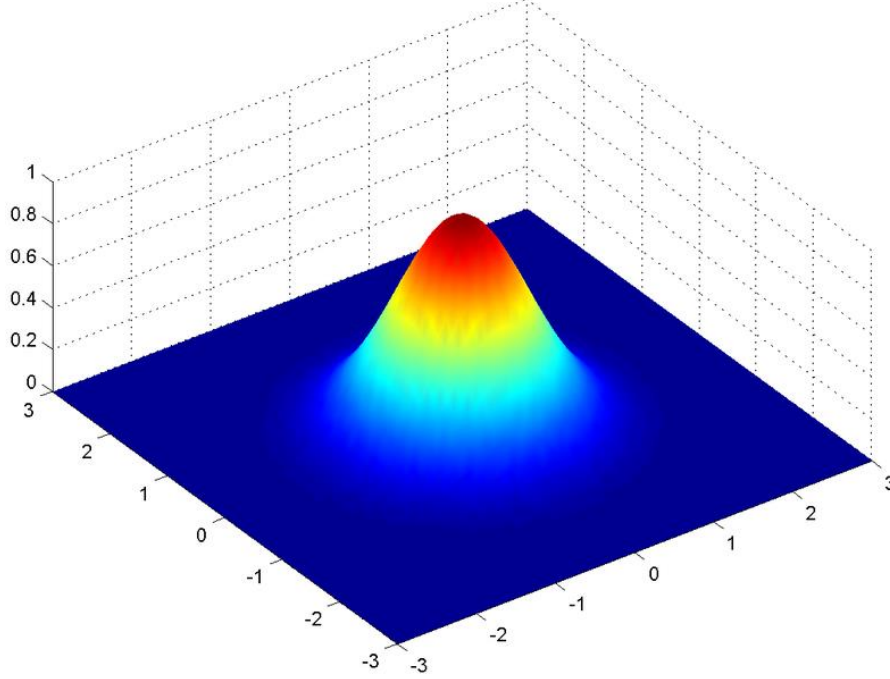


Figure 4.1 A 2-D Gaussian curve

## 4.2 Approximation of VHS via Gaussian Functions

The gray values for organs of interest have varying intensity ranges and characteristics even for the same organ in different MRI acquisitions. However, by evaluating VHS with respect to different MR sequences, some common characteristic properties are observed in VHS. One of them is that VHS becomes narrower at the beginning or end slices and widens in the middle slices. It should be noted that the use of DICOM image series, which supply large numbers of gray levels, is necessary to obtain a compact desired histogram. The other important point is that the desired histogram should be distinguishable from the unwanted components/tissues. This distinction in VHS generates two valleys in both sides of the VHS. Figure 4.2 illustrates some resultant histograms, which are obtained using the developed GUI, along with their desired counterparts.

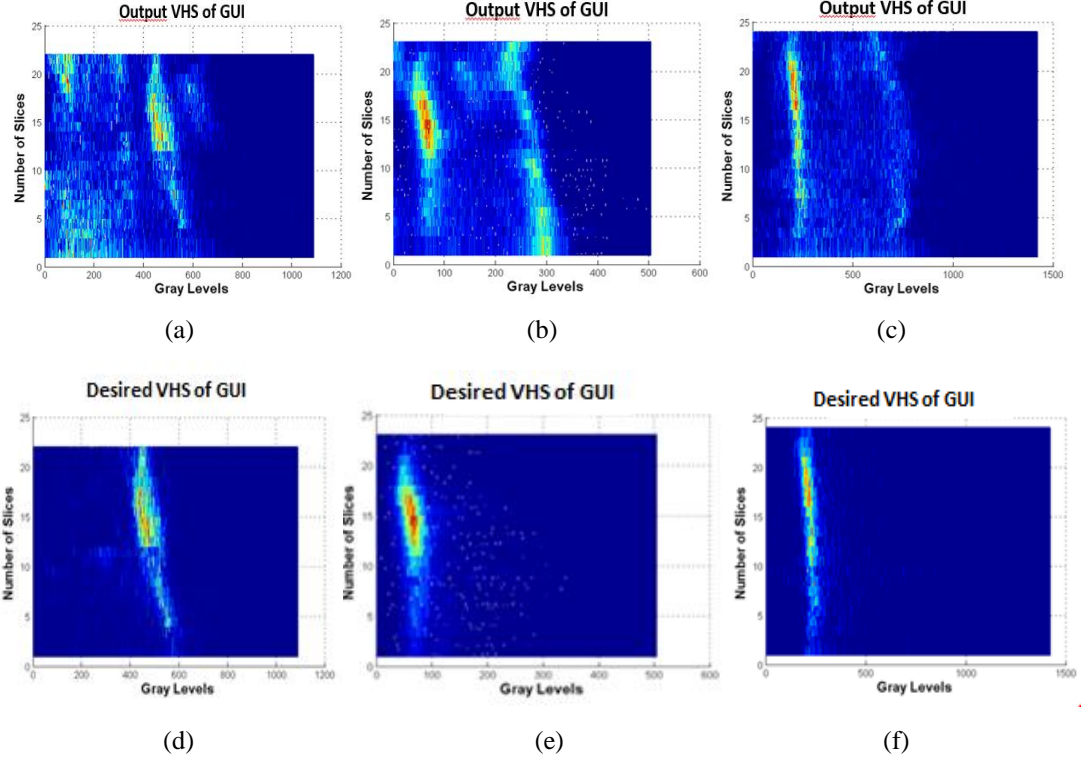


Figure 4.2 (a)-(c) Top view of resultant VHS of the GUI (d)-(f) Top view of their respective desired counterparts

The VHS should be modeled in order to determine the valleys in a robust manner. The selection of the lobes from the VHS requires an approximation to obtain the desired lobe. For modeling a VHS, some important issues must be taken into account. One of them is the non-smooth structure of VHS because of the intensity fluctuations of MRI. The second problem is the variability in the gray level range of the same organ among slices. In MRI imaging, an organ of interest might have a varying intensity range through the slices. The third problem is the slice thickness of the MRI data. This thickness causes a limited sampling in z-direction and results in a high inter-slice distance.

The shape of the VHS is like a bell curve with a certain radius and intensity. In the center of the VHS, there exist a lot of pixels that create high amplitude bells, each of which is called a “lobe”. Gaussian function is a good approximation for fitting the lobes of VHS. Besides, defining the VHS in terms of Gaussian functions provides an intuitive initial TF design employing the parameters of Gaussian function.

Representation of all the lobes in the VHS with Gaussian functions is a crucial step of the approximation process. As more lobes are fitted, a better approximation is obtained.

For fitting the lobes of the VHS, we utilize a special type of Gaussian function which is also known as 2-D Morlet wavelet function in the literature (Antoine & Murenzi, 1996). It is defined as

$$g(x, y) = e^{-1/2(\varepsilon^{-1}x^2 + y^2)} \quad (4.3)$$

where  $\varepsilon$  is called the elongation parameter. For  $\varepsilon > 1$ , modulus of  $g(x, y)$  is elongated along the  $x$  direction. In our calculations, we fixed the value of  $\varepsilon$  as 15. By considering the general structure of the VHS, the above value of  $\varepsilon$  is determined to be the most appropriate among other values.

For approximating the lobes of the VHS, rotation and axis scaling operations are applied to the elongated prototype Gaussian function in Equation 4.3. The applied rotation and axis scaling transformations can be defined together as

$$\begin{pmatrix} x' \\ y' \end{pmatrix} = \frac{1}{a} \begin{pmatrix} \cos \theta & \sin \theta \\ -\sin \theta & \cos \theta \end{pmatrix} \begin{pmatrix} x \\ y \end{pmatrix} \quad (4.4)$$

where  $x'$  and  $y'$  are the rotated axes in the clockwise direction by  $\theta$ . The axes are scaled by the parameter,  $a$ , which directly affects the support region of the Gaussian function.

#### ***4.2.1 Gaussian Parameters and Orientations***

Various possible Gaussian basis functions can be created as a filter bank employing multiple orientation and scale values. As seen in Equation 4.4, variable  $a$  is the axis scaling parameter of the transformation. The rotation variable  $\theta$  controls

the orientation and has a critical importance on finding the appropriate basis function that fits the corresponding lobe of the VHS. Figure 4.3 shows the top and side views of the Gaussian basis functions which have the same  $a$  and  $\varepsilon$  parameters, but different  $\theta$  parameter values. Figure 4.4 shows the filter bank of the Gaussian basis functions with respect to different scale and angle parameters.

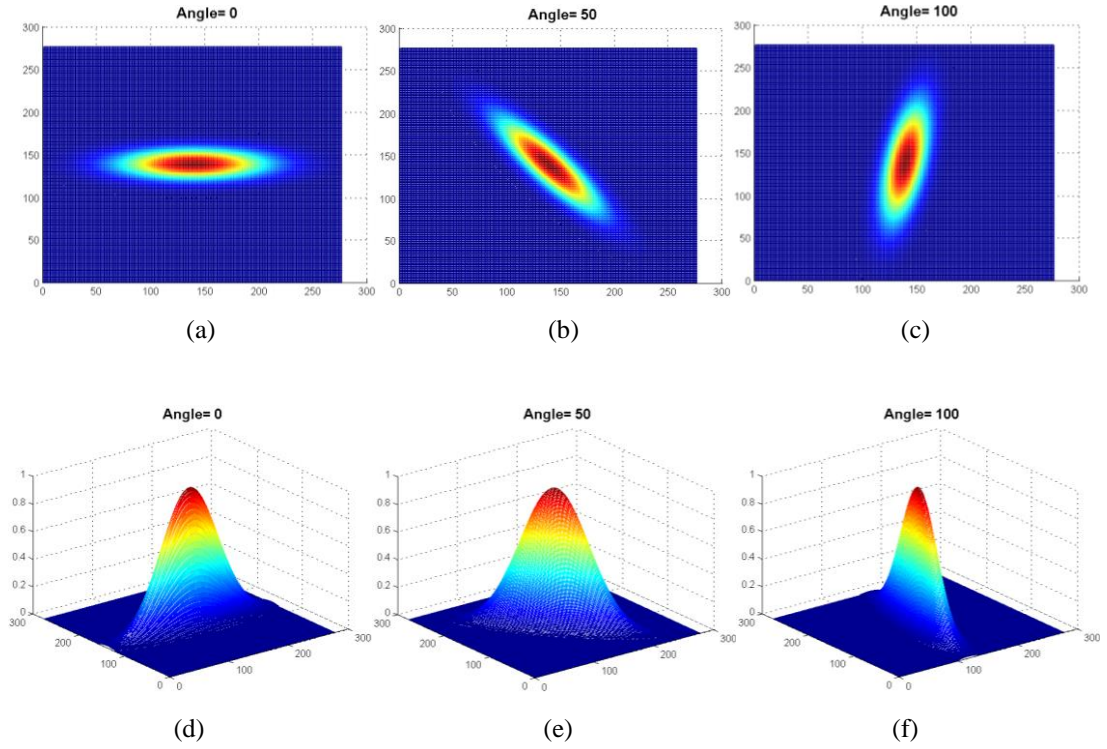


Figure 4.3 2-D Gaussian functions with respect to different angles (a)-(c) Top view (d)-(f) Side view

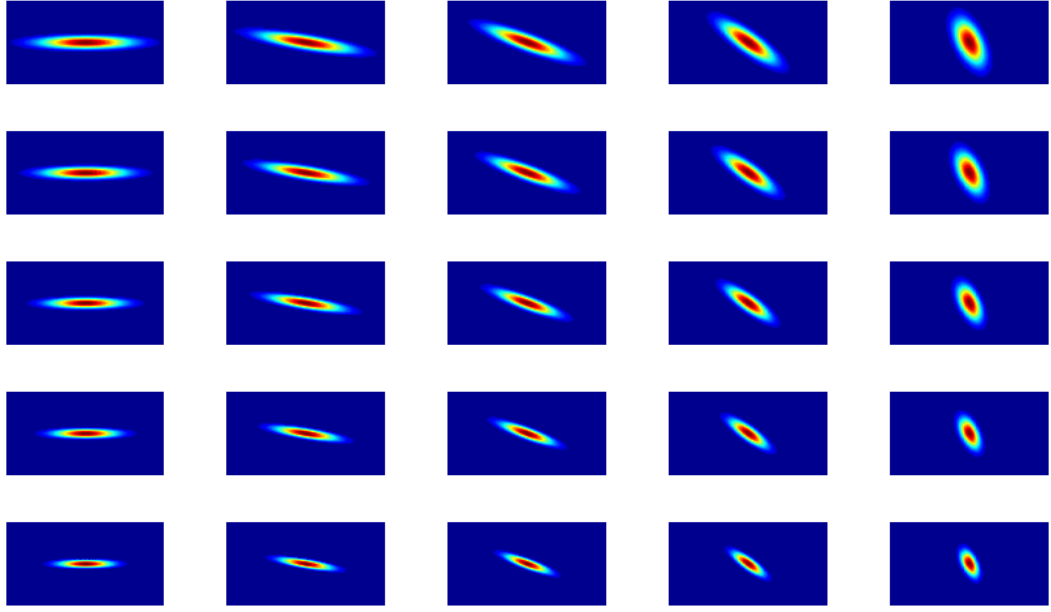


Figure 4.4 Filterbank of Gaussian basis functions (each row corresponds to a certain scale and each column corresponds to a certain orientation)

Using Equation 4.4, a rotated and axis scaled Gaussian basis function can be expressed with respect to given  $a$ ,  $\theta$ , and  $\varepsilon$  parameters as follows;

$$g_{a,\theta}(x', y') = e^{-1/2(\varepsilon^{-1}(a^2(x'\cos\theta - y'\sin\theta)^2) + a^2(x'\sin\theta - y'\cos\theta)^2)} . \quad (4.5)$$

Note that the prototype Gaussian function in Equation 4.3 corresponds to the special case of  $g_{1,0}(x, y)$  which consists of no axis scaling and no rotation.

It has been already mentioned that VHS structure can be approximated by Gaussian basis functions. Therefore, using fixed scale and/or rotation parameters in the approximation causes losses in determining small or suppressed lobes in data. Especially, fitting only the major lobes results with losses in the beginning/end slices and fitting only the minor lobes causes over-fitting to the unwanted components. These drawbacks should be taken into careful consideration and an optimal set of parameters that would be useful for both major and minor lobes, which contain detailed information about the organ of interest, should be used.



In this study, by considering the above mentioned criteria, a hierarchical and multi-scale modeling is proposed. In an iterative manner, the proposed model tries to find the best Gaussian basis to fit the corresponding lobe of the VHS. The developed algorithm provides a procedure for capturing all suppressed lobes of importance in a successive manner by associating the lobes with a suitable number of Gaussian basis functions.

Using different scales provides the user with the convenience of expressing different lobes in the right way. However, the characteristics of VHS demonstrate that lobes can have curvy structures. The best approximation for these curvy parts is to integrate the rotation parameter to the algorithm as an extra degree of freedom. For a fixed scale parameter, the best rotation parameter is determined through the calculation of correlation between the Gaussian basis functions and VHS. Correlation can be calculated in an easier way in the frequency domain by multiplying the Fourier transform of the VHS by the conjugate of the Fourier transform of the Gaussian basis function.

Let us denote our final approximated VHS as  $VHS(x, y)$  which is formed by combining all approximating Gaussian basis functions in an additive manner. However, before combining the suitable Gaussian basis functions, the best rotation angle among all possible choices of angles must be determined in an iterative manner. Here, each iteration corresponds to a different scale. Iterations start from the largest scale value and continue until the smallest scale value in a hierarchical manner. In our simulations, we used 8 different scale values. Thus, denoting the number of iterations by  $N$ , we have  $N = 8$ . For each scale,  $\theta$  is varied from 0 up to a maximum of 170 degrees with an increment of 10 degrees. Thus,  $\theta = \{0, 10, \dots, 170\}$  defines the vector of rotations. Denoting the length of the vector,  $\theta$ , by  $M$ , we have  $M = 18$ .  $Corr\{\cdot\}$  is defined as the 2-D correlation operation between Gaussian basis function,  $g_{a_i, \theta_j}(x', y')$ , and the VHS which is represented by  $VHS(x, y)$ . For a fixed scale, the correlation is calculated for different rotations as:

$$\text{Corr}_j = \text{Corr} \left\{ g_{a_i, \theta_j}(x', y'), VHS(x, y) \right\} \quad (4.6)$$

In Equation 4.7, we represent the best rotation angle as  $\hat{\theta}$  which corresponds to the maximum correlation between VHS and Gaussian basis functions.

$$\hat{\theta} = \arg \max_{\theta_j} \left( \text{Corr} \left\{ g_{a_i, \theta_j}(x', y'), VHS(x, y) \right\} \right)_{j=1}^M \quad (4.7)$$

We can express our approximated  $VHS(x, y)$  as a weighted summation of the rotated and axis scaled Gaussian basis functions,  $g_{a_i, \theta_j}(x', y')$ .

$$VHS(x, y) = \sum_{i=1}^N \sum_{j=1}^M w_j g_{a_i, \theta_j}(x', y') \quad (4.8)$$

$$\text{where } w_j = \begin{cases} 1 ; & \text{max correlation for scale } a_i \text{ among all possible } \theta_j \text{ angles} \\ 0 ; & \text{for the rest of the } \theta_j \text{ angles} \end{cases}$$

#### 4.2.2 Implementation of Gaussian Approximation Model

The model associated with each feature includes a large number of intrinsic parameters (gray level intensities, position and orientation of the feature etc.). Having the approximation model that suitably describes our features of interest; we are now interested in applying this model to our data. Our problem is to find the best parameters that characterize the model and to make it fit as well as possible to the data at hand. Our approach provides a multi-scale procedure for capturing all lobes of the data.

It has already been noted that an MR series (such as T1-DUAL, T1-WATS, T2-SPIR, except the THRIVE sequence) consist of approximately 25 images. By considering the gray levels of DICOM images, maximum value reaches up to 1600 gray levels. Thus, VHS becomes a matrix whose width is 25 and height is 1600.

There is an incompatibility between the dimensions of the VHS. To overcome this incompatibility, simple linear interpolation is applied to the width of the VHS.

Our hierarchical multi-scale method decreases the scale of the approximating Gaussian basis functions at each iteration of the proposed algorithm. It is expected and aimed that first the larger lobes of the VHS are detected. However, a large scale Gaussian basis function also requires a larger support region. At each iteration, in parallel to the decrease of the scale, the support regions of the Gaussian basis functions also decrease proportionally. On the other hand, the DICOM images used in the study are 16-bit images causing a variation in the maximum gray level from 256 up to 65536. This means that using a fixed support region is not suitable for all scales. Instead, different gray level value ranges or different dynamic ranges require different scales and support regions. By evaluating the dataset of each sequence used in this study, the gray level ranges are defined as follows:

$$\begin{aligned}
1400 \leq x \leq 1800 & \Rightarrow x \in \text{Region 1} \\
1000 \leq x < 1400 & \Rightarrow x \in \text{Region 2} \\
700 \leq x < 1000 & \Rightarrow x \in \text{Region 3} \\
400 \leq x < 700 & \Rightarrow x \in \text{Region 4}
\end{aligned}$$

It is not suitable to fit Gaussian basis functions having the same scale parameter for different regions defined above. Therefore, for each separate region, the scale set is multiplied by a constant associated with the corresponding region. The support region of the Gaussian basis function is always less than the size of the VHS. Therefore, a matrix, which has the same size with the VHS, is constructed and the Gaussian function is placed in the middle of that matrix. Then, VHS and Gaussian function are transferred to the frequency domain using the Fourier transform. It is known that multiplying the Fourier transform of the image by the conjugate of the Fourier transform of Gaussian basis function in the frequency domain corresponds to correlation. Normalizing and getting the absolute value of the result give the normalized absolute correlation between the Gaussian basis function and the VHS.

In the main algorithm, what is important is to find the maximum point of the VHS corresponding to a major lobe in the original data. However, the found maximum point may not define the major lobe of the VHS. To overcome this problem, when the Gaussian basis function is fitted to the VHS, it is checked whether the support region of the Gaussian basis function exceeds the border of the VHS. If the exceeding of the border of VHS occurs then the same algorithm is applied to the second maximum point of the VHS. This procedure repeats itself until all maximum points, which do not exceed the borders of the VHS data, are found.

After finding an appropriate maximum point or points, correlation results, which have already been calculated with respect to different rotations, are used to approximate the VHS. Based on the maximum point, the approximating Gaussian basis function is determined according to the correlation values among different rotations. At each scale, the support region of the approximating Gaussian basis function in VHS data is obtained. The values of the VHS corresponding to the support region of the Gaussian basis function are added. This summation defines the criterion for fitting more than one Gaussian basis functions in the same scale. After finding the appropriate Gaussian basis function, the approximated Gaussian is removed from the VHS data. As removing operation, we set 0 to the VHS data where the support region of the approximating Gaussian basis function exists. In Equation 4.9 below the residual data is defined as  $r(x, y)$ ;

$$r(x, y) = VHS(x, y) - g_{a_i, \hat{\theta}}(x', y') \quad (4.9)$$

Until this step only one Gaussian basis function defines the original data. There is an 80% criterion for fitting multiple Gaussian functions during the same scale. For obtaining the support region of the Gaussian function, we define an operation called  $\text{SupReg}\{\mu_{x_n}, \mu_{y_n}\}$ .  $\mu_{x_n}$  and  $\mu_{y_n}$  correspond to the mean values of the Gaussian basis function which is compared with the first Gaussian basis function. The mean values of the Gaussian define where the Gaussian is fitted in the VHS data. And also, by knowing the mean values, the support region of the Gaussian can be calculated and

compared with the first Gaussian basis function. The support region operation is defined as;

$$\text{SupReg}\{\mu_x, \mu_y\} = \begin{cases} 1; & \left| \sigma_{g_{\alpha_i, \hat{\theta}}} \right| > 0.05 \\ 0; & \text{otherwise} \end{cases} \quad (4.10)$$

For representing summation operation we simply define the operation  $\text{sum}\{ \}$  which adds all the values in a matrix or vector.

The correlation operation is repeated again but this time the input becomes the residual data  $r(x, y)$  instead of  $VHS(x, y)$ . Other Gaussian basis functions are obtained after they are compared with the given criterion. The Gaussian basis functions which comply with the given criterion are fitted to the VHS. If there is no Gaussians satisfying the criterion, then it can be stated that there is only one fitting Gaussian basis function at that particular scale. This criterion provides the user with the convenience of fitting more than one Gaussian functions in the same scale in order to express the lobes of the VHS whose heights are almost the same. The following pseudo code in the next page shows the iterative and hierarchical nature of the algorithm by paying attention to the approximation criteria with respect to different scale and rotation parameters.

Our developed approach provides a multi-step procedure for capturing all suppressed lobes of importance in a successive manner by associating the lobes with appropriate number of Gaussian bases. At each iteration, the position and the angle of each Gaussian function is extracted. This means that these functions express the VHS data in an approximate fashion. After fitting Gaussian functions, the lobes which correspond to these functions, are set to zero. The next approximation considers the residual VHS found at the previous iteration as the new function to be approximated and the number of Gaussians and their parameters are calculated now for that residual.

At each scale, more than one Gaussian function can be found to approximate the VHS data. Our main approach is first to catch the major lobes and then the minor lobes. Therefore, the scale parameter has its maximum value at the first iteration and starts to decrease as the iteration number increases. All Gaussian functions are combined in one matrix and thus the final approximation is obtained. Figure 4.5 shows the approximation procedure step by step and the resultant final approximation.

```

 $r(x, y) = VHS(x, y)$ 
 $VHS(x, y) = 0$ 
for  $i = 1 : N$ 
    for  $j = 1 : M$ 
         $Corr_j = Corr\{g_{a_i, \theta_j}(x', y'), r(x, y)\}$ 
    end
     $\hat{\theta} = \arg \max_{\theta_j} \left( Corr\{g_{a_i, \theta_j}(x', y'), r(x, y)\} \right)_{j=1}^M$ 
     $r(x, y) = r(x, y) - g_{a_i, \hat{\theta}}(x', y')$ 
     $\overline{VHS}(x, y) = \overline{VHS}(x, y) + g_{a_i, \hat{\theta}}(x', y')$ 
    n=1
    while(1)
        for  $j = 1 : M$ 
             $Corr_j = Corr\{g_{a_i, \theta_j}(x', y'), r(x, y)\}$ 
        end
         $\hat{\theta}_n = \arg \max_{\theta_j} \left( Corr\{g_{a_i, \theta_j}(x', y'), r(x, y)\} \right)_{j=1}^M$ 
        if  $\sum \{r(x, y) * Sup Re g\{\mu_x, \mu_y\}\} > g_{a_i, \hat{\theta}}(x', y') * 0.8$ 
             $r(x, y) = r(x, y) - g_{a_i, \hat{\theta}_n}(x', y')$ 
             $\overline{VHS}(x, y) = \overline{VHS}(x, y) + g_{a_i, \hat{\theta}_n}(x', y')$ 
            n=n+1
        else
            break
        end
    end
end
end

```

To approximate the VHS, this procedure continues for 8 iterations by default, since it is observed in the simulations that 8 iterations are sufficient in most cases. Of course, it can be further iterated if the generated Gaussian basis functions are not considered enough to construct an appropriate TF by the user and until a satisfactory number of units is obtained. The advantage of this coarse-to-fine fitting approximation is that it can be stopped at the desired level of accuracy without having to deal with any further fine details.

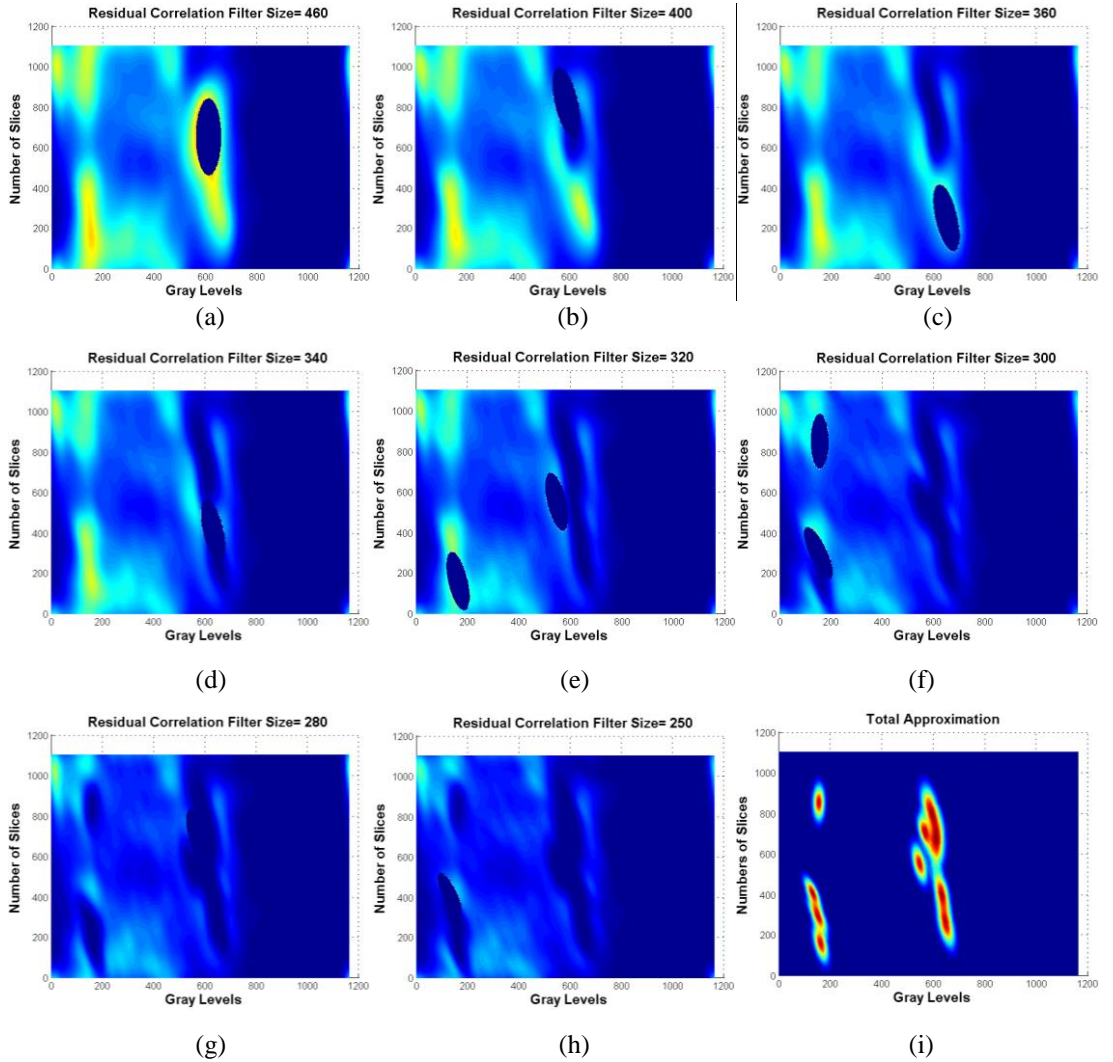


Figure 4.5 Each labeled part of (a-h) represents the residual correlation between VHS and the Gaussian kernel in different scales after fitting with an appropriate filter size and angle. (i) Final approximation with all Gaussian functions

### 4.2.3 The Thresholding Process

After approximating the VHS, a method should be used to threshold the approximated VHS by determining the two valleys so that upper and lower thresholds can be determined correctly. Our main goal is to determine the two threshold values which correspond to the valleys at the left and right sides of the corresponding lobe of the organ of interest. As stated before, the main idea behind the Gaussian modeling is to find the basis functions that best fit the desired lobes and then to determine a threshold range to express the region of interest in the VHS. Thus, after the Gaussian fitting step, as seen in Figure 4.5, the gray levels which belong to the organ of interest are grouped together as shown in Figure 4.6 (a). The center of the group is indicated by the mean of the gray levels, which are obtained via points through which the spline passes. The points, at which the tail of each Gaussian becomes zero, indicate the threshold range. As seen in Figure 4.6 (b), a varying threshold range can be obtained using the Gaussian bases which are found by the multi-scale hierarchical model. The flowchart of the proposed method is given in Figure 4.7.

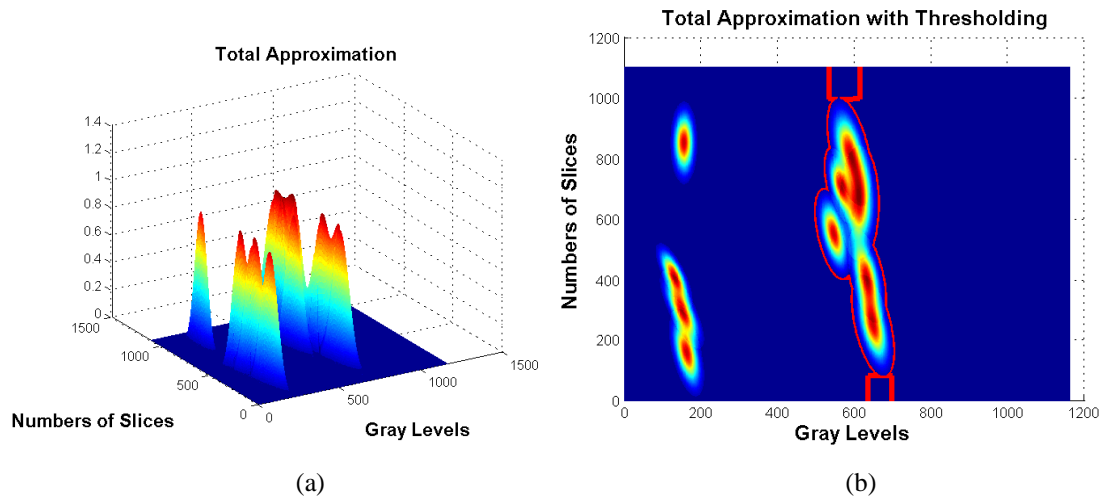


Figure 4.6 (a) The resultant approximating Gaussian functions (b) Top view of the resultant approximation of Gaussian functions with a varying threshold range represented by red lines



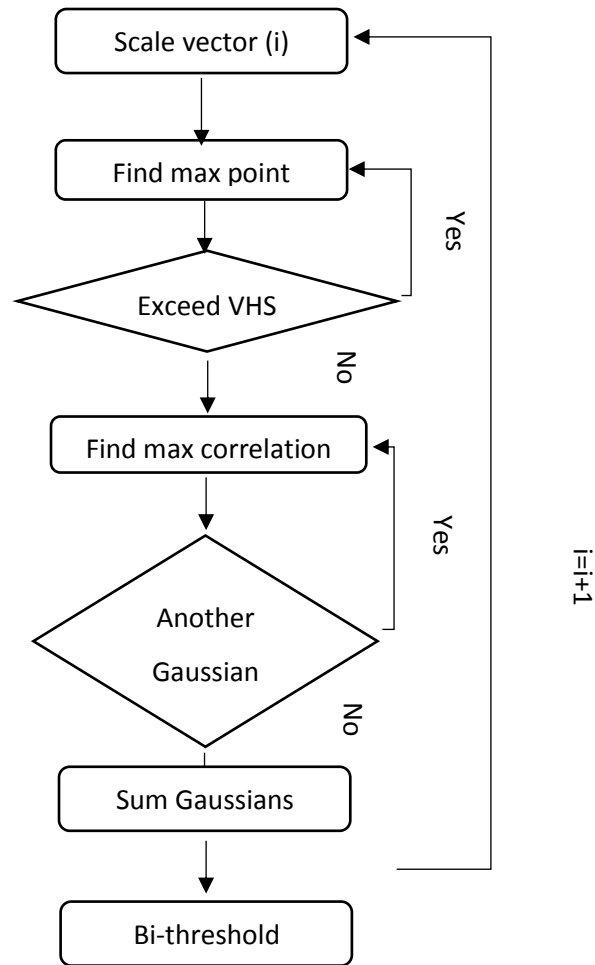


Figure 4.7 The flowchart of the Gaussian modeling process.

#### 4.2.4 Morphological Operations

Morphological operations in image processing are a collection of non-linear operations related to the shape or morphology of features in an image. Morphological operations rely only on the relative ordering of pixel values, not on their numerical values, and therefore are especially suited to the processing of binary images. Morphological operations can also be applied to grayscale images whose light transfer functions are unknown and therefore their absolute pixel values are of no or minor interest.

Morphological techniques probe an image with a small shape or template called a structuring element. The structuring element is positioned at all possible locations

in the image and compared with the corresponding neighborhood of pixels. Some operations test whether the element “fits” within the neighborhood, while others test whether it “hits” or intersects the neighborhood as seen in Figure 4.8 (Efford, 2000).

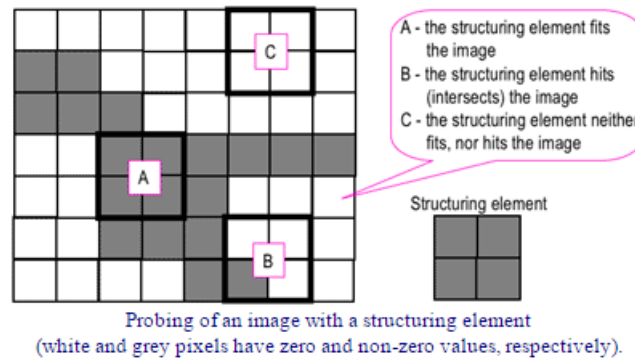


Figure 4.8 Implementation of the structuring element in an image

The structuring element is a small binary image, i.e. a small matrix of pixels, each with a value of zero or one:

- The matrix dimensions specify the *size* of the structuring element.
- The pattern of ones and zeros specifies the *shape* of the structuring element.
- An *origin* of the structuring element is usually one of its pixels, although generally the origin can be outside the structuring element.

#### 4.2.4.1 Implementation of the Morphological Operations

One of the most challenging problems following approximation is that adjacent organs and tissues have quite similar gray level intensities with the liver. To overcome this problem, we decided to apply morphological operations to our dataset. Erosion, largest connected component, and dilation are utilized as morphological operations, respectively. Dilation adds pixels to the boundaries of objects in an image, while erosion removes pixels on object boundaries. The number of pixels added or removed in an image depends on the size and shape of the *structuring element* used to process the image. In the morphological dilation and erosion operations, the state of any given pixel in the resultant image is determined by

applying a rule to the corresponding pixel and its neighbors in the input image. The rule used to process the pixels defines the operation as dilation or erosion.

Indicating the order of morphological operations is a significant and critical step in morphology. The main reason of the importance of this ordering is that erosion and dilation operators could have some drawbacks when applied in an incorrect order. Considering our problem, which is gray level similarity between liver and adjacent organs such as kidney, the first operation is the erosion to break the connection between the lower part of the liver and the right kidney and between the upper part of the liver and the heart and/or any other tissue which have connections. At the first step, connections between the liver and any other tissue are broken. Each disconnection creates separate components from one combined component. The second step is finding the largest connected component in the image slice. In the middle slices of the dataset liver becomes the largest organ but in the beginning/ending slices the liver becomes smaller. Thus, applying 3-D largest connected component to the dataset is the best way to keep the liver as the largest organ in the dataset. The last step is the dilation step to get back the pixels of the liver which might have been lost during erosion operation.

Before these operations, determining the appropriate structuring element is one of the most crucial steps of the morphological operation. During determination of the appropriate structuring element, the smooth and oval structure of the liver should be taken into account. In light of this information and considering the shape of the liver, two structuring elements are defined. The first structuring element is a line whose length is 5 pixels and angle is  $45^{\circ}$  degrees from the horizontal axis. The second structuring element is a 3-D function of  $\ln x$  as shown in Figure 4.9.

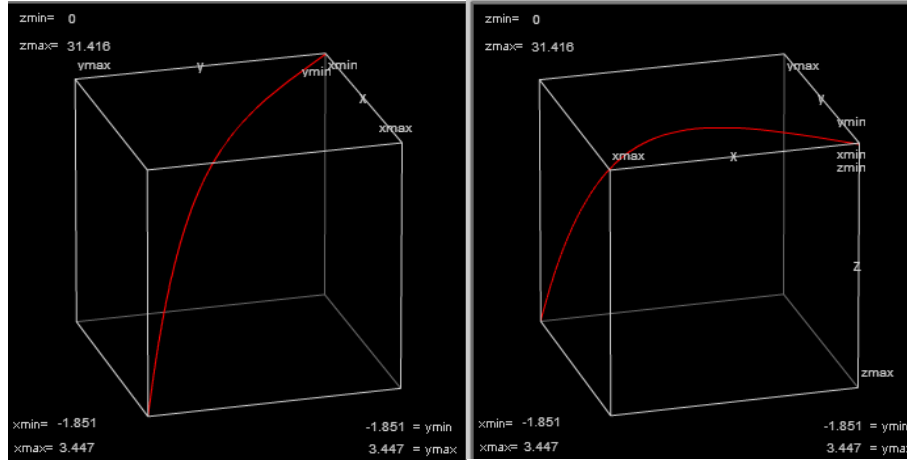


Figure 4.9 3-D structuring element as observed from different angles

During the erosion step, the 2-D structuring element is applied to each 2-D image slice of the dataset. However, the 3-D structuring element is only applied to the lower part of the 3-D dataset to break the connections between the liver and the right kidney. Applying the 3-D  $\ln x$  function to the whole data causes large pixel losses in the dataset. During dilation step, the lower part of the dataset is dilated using 3-D  $\ln x$  function after the 2-D image slices of the dataset are dilated with a 2-D structuring element.

#### 4.2.5 Region Growing

Region growing is a simple region-based image segmentation method. It is also classified as a pixel-based image segmentation method since it involves the selection of initial seed points. This approach to segmentation examines neighboring pixels of initial seed points and determines whether the pixel neighbors should be added to the region.

After performing morphological operations, the pixels which belong to liver in each 2-D image slice of the dataset are defined as the initial seed points of the region growing segmentation method. The initial seed points might vary for each image slice in the same dataset. The region growing starts from a seed point by comparing it with neighboring pixels. Region grows starting from the seed pixel by adding the neighboring pixels that are similar, increasing the size of the region. Therefore, if

neighboring pixels have similarity in grey level with the liver then the region keeps growing and it might exceed the boundaries of the liver. To overcome this problem, the pixels of the liver which express the information of the liver boundary are discarded from the seed point cluster.

## CHAPTER FIVE

### APPLICATION AND RESULTS

During the fitting of the Gaussian functions to the lobes of VHS, non-smooth characteristic structure of VHS and the difficulty of working with MRI must be taken into account. One of those difficulties is the irregular rising and falling of intensity in MR imaging preventing smoothness. The second problem is the variation of gray levels for the same organ among different sequences. Due to this fact, gray levels cannot be restricted to a certain range. Thus, the intensity range of the organ of interest can have completely different gray levels for different sequences. The third problem is the slice thickness of MRI dataset that causes a limited sampling in  $z$ -direction and results in a high inter-slice distance.

Our segmentation results are evaluated using the average error rate (AER) (Seo, Ludeman, Park, & Park, 2004). AER is defined as the area difference between the region segmented by the algorithm ( $RA$ ) and the region segmented manually ( $RM$ ). Defining a union region  $RU$  as  $RA \cup RM$  and an intersection region  $RI$  as  $RA \cap RM$ , volumetric overlap error ( $VOE$ ) is given in Equation 5.1. AER is similar to  $VOE$  criterion which is used in (Ginneken, Heimann, & Styner, 2007). In the evaluation, 0 value of  $VOE$  indicates perfect segmentation, with no limitation for any upper bound for the  $VOE$  value.

$$VOE = \frac{RU - RI}{RU} \times 100 \quad (5.1)$$

Some examples of different sequences of MPR images are given in Figure 5.1. Red pixels show True Positive (TP) pixels after the thresholding process. This means that the red pixels are classified as the organ of interest and these pixels are actual organ pixels. Therefore, it can be stated that by using Gaussian approximations and the thresholding process, the segmentation of the organ is accomplished substantially. Green pixels of the images represent the organ pixels which are not found by our algorithm. And lastly, blue pixels are the pixels which belong to the

unwanted pixels/adjacent tissues but are found as belonging to the organ by our algorithm. Observing Figure 5.1, we see that there is not a direct relation among different sequences. However, if a number of slices of the image series are observed, it can be stated that using coarse approximation at the first and last slices is not enough for segmentation. In contrast to the first and last slices, in the middle of the image series our algorithm provides a better approximation.

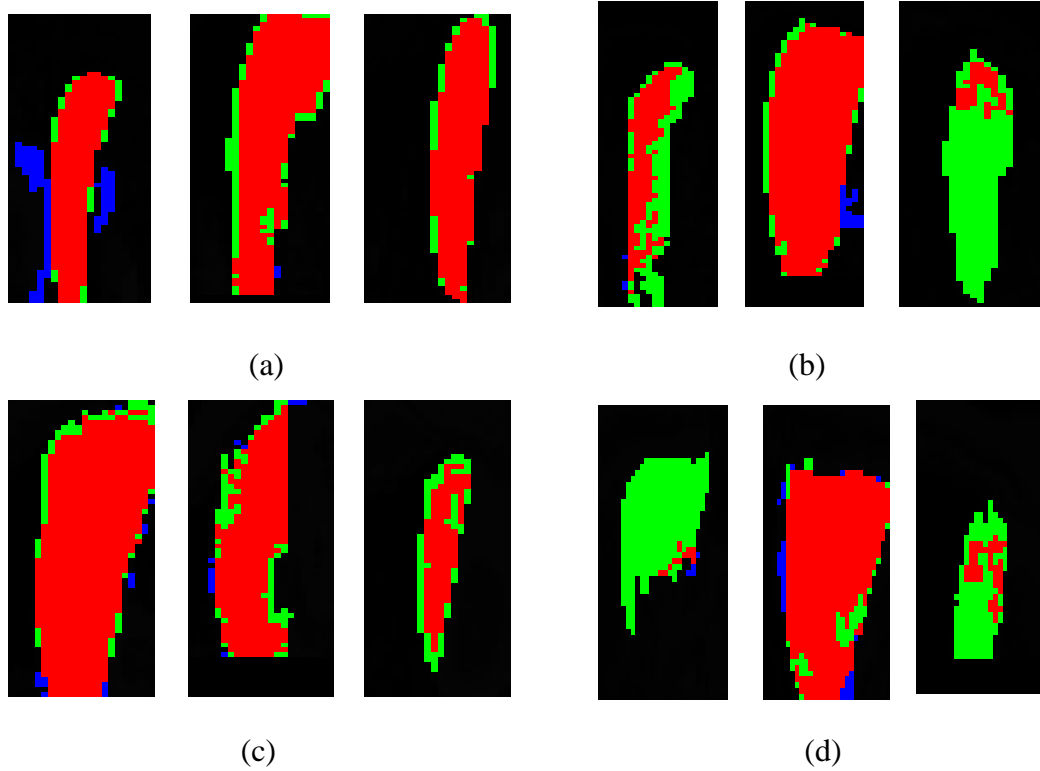


Figure 5.1 MPR images belonging to T1 WATS with slice numbers (a) 3-11-21 and (b) 2-13-21. MPR images belonging to T1-DUAL with slice numbers (c) 12-18-24 and (d) 2-10-22.

Our proposed algorithm is applied to 5 different MR sequences. SSH and T2-SPIR sequences generally generate dark images which cannot be distinguished from the outer region and adjacent pixels. The organ of interest and non-object gray levels overlap each other and it is not possible to identify a threshold range on the overlapping region. Therefore, T1-DUAL, THRIVE, and T1-WATS sequences are chosen for the study.

The numbers of analyzed datasets of sequences are given in Table 5.1. Firstly, the algorithm is applied to all images in the dataset. Secondly, the first and the last 5

images in the analyzed dataset are ignored. For the last approach, the first 8 and the last 2 images are ignored. In the evaluation, 0 value of *VOE* indicates perfect segmentation and there is no limitation for the upper value of the *VOE*. At the beginning of the MR series, the organ of interest does not exist and by going forward in slices, organ starts to appear. In the middle of the image series, the organ takes its largest volume. At the end of the image series, the organ starts to disappear. Therefore, at the beginning and end of the series, VHS becomes narrow. In contrast, in the middle, VHS takes a larger part and the grey level information of the organ of interest from VHS can be expressed in an accurate way by using Gaussian approximations.

Because of the structure of VHS, our algorithm gives better results in the middle slices. Therefore, the other images are ignored in the calculation of *VOE*. For the initial and final images, refinement algorithm can be developed to capture pixels which have low amplitudes and are spread in VHS. As seen in Table 5.1, T1-WATS and THRIVE sequences have lowest overlapping error. THRIVE and T1-WATS sequences are obtained by scanning liver consecutively in a short time with thin slices to get response of a known lesion to a contrast matter. That is why these sequences provide a signal increase caused by contrast matter instead of image quality. This fact decreases *VOE* and creates a distinguishable grey level difference between the organ of interest and non-object pixels in VHS.



Table 5.1 *VOE* results with respect to MR sequences

Sequences	Number of dataset	Volumetric Overlap Error (VOE)		
		All Dataset	First 5 Last 5 ignored	First 8 Last 2 ignored
<b>T1-DUAL</b>	5	37.18	26.89	24.28
<b>THRIVE</b>	2	32.41	23.72	19.16
<b>T1-WATS</b>	6	36.55	23.85	18.97

By using Gaussian approximations and the thresholding process, we have significant improvements on MPR images in the middle slices of the dataset. However, beginning and end image slices give important information about 3-D volumetric data. To enhance the approximation and obtain meaningful information from beginning and end slices, morphological operations and region growing segmentation methods are applied to the images as described in Sections 4.2.4 and 4.2.5, respectively. Section 2.4 describes all datasets used. However, some of the datasets are eliminated which are not suitable for our algorithm. Therefore, after the enhancement procedure, the algorithm is applied to 29 (14 T1 DUAL+10 T1 WATS+5 THRIVE) MRI datasets in this thesis work. For visualization, instead of using MPR images, we utilized the axial images to observe the achievement of our algorithm. Figures 5.2 and 5.3 show the axial image slices with respect to different sequences before morphological operations. Tables 5.2 through 5.4 show metric results with respect to different sequences before morphological operations.

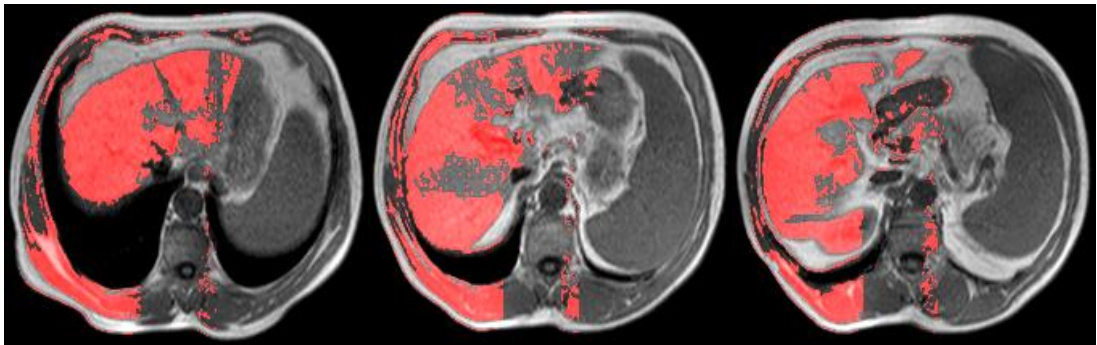


Figure 5.2 Different axial image slices belonging to T1 DUAL before morphological operations.

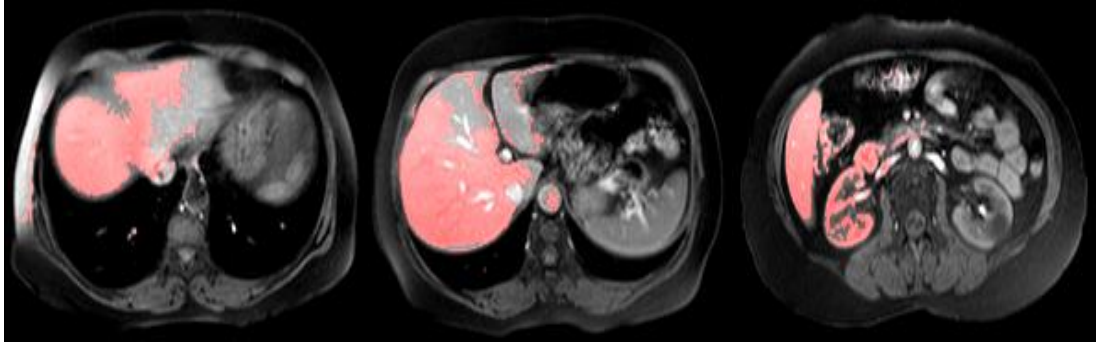


Figure 5.3 Different axial image slices belonging to T1 WATS before morphological operations.

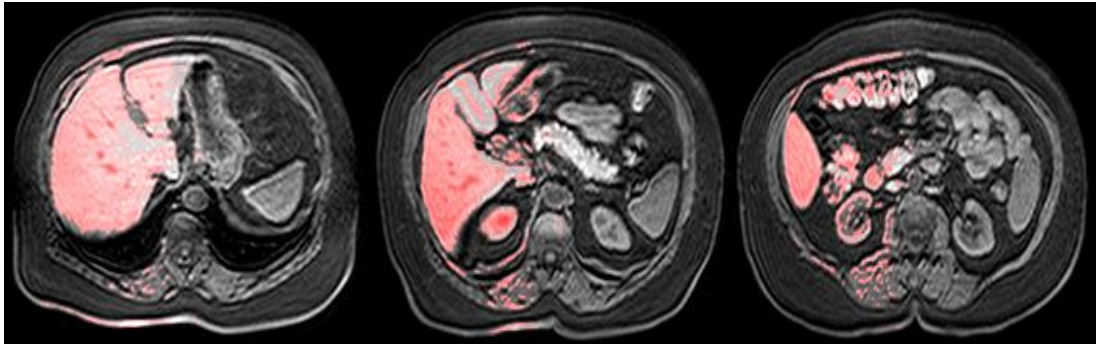


Figure 5.4 Different axial image slices belonging to THRIVE before morphological operations.

Table 5.2 Metric results of T1 DUAL sequence with respect to the dataset

Dataset	CC	FP	FN	SE	SP	PPV	NPV
2	91.79	4.25	71.71	28.29	95.85	30.38	95.43
3	93.49	4.17	54.07	45.93	95.90	36.30	97.21
4	95.97	1.89	58.47	41.53	98.12	46.60	97.70
5	93.78	3.52	57.53	42.47	96.52	39.51	96.91
6	94.82	3.50	48.55	51.45	96.55	37.32	98.03
7	93.71	4.07	54.80	45.20	96.00	34.83	97.37
10	97.70	1.14	39.84	60.16	98.85	61.64	98.78
11	94.27	4.78	42.36	57.64	95.36	27.09	98.69
12	94.09	4.64	56.61	43.39	95.51	21.31	98.37
13	93.83	4.96	54.08	45.92	95.21	21.59	98.39
16	95.30	2.89	48.85	51.15	97.13	42.52	97.95
17	93.21	5.03	41.51	58.49	95.06	38.73	97.72
18	92.70	6.11	57.71	42.29	94.17	17.42	98.25
19	95.23	2.23	48.16	51.84	97.76	57.41	97.21
20	91.58	7.53	48.06	51.94	92.88	19.31	98.33
21	93.02	5.85	53.21	46.79	94.39	19.82	98.36
Ave*	94.03	4.16	52.22	47.78	95.95	34.49	97.79

Ave\*: Average

Table 5.3 Metric results of T1 WATS sequence with respect to the dataset

<b>Dataset</b>	<b>CC</b>	<b>FP</b>	<b>FN</b>	<b>SE</b>	<b>SP</b>	<b>PPV</b>	<b>NPV</b>
<b>2</b>	93.81	2.95	65.92	34.08	97.08	39.08	96.41
<b>3</b>	96.53	1.24	56.60	43.40	98.76	59.37	97.66
<b>7</b>	95.49	1.63	71.43	28.57	98.38	43.19	96.96
<b>10</b>	96.01	1.10	54.92	45.08	98.88	69.46	96.96
<b>16</b>	96.43	1.42	53.46	46.54	98.57	58.24	97.73
<b>17</b>	96.15	1.38	51.42	48.58	98.60	64.14	97.38
<b>18</b>	96.48	2.07	78.82	21.18	97.97	17.00	98.44
<b>19</b>	95.01	2.02	62.57	37.43	97.98	48.94	96.81
<b>20</b>	94.89	2.58	72.75	27.25	97.46	28.97	97.24
<b>21</b>	95.65	2.32	77.58	22.42	97.72	21.71	97.81
<b>Ave*</b>	95.65	1.87	64.55	35.45	98.14	45.01	97.34

Table 5.4 Metric results of THRIVE sequence with respect to the dataset

<b>Dataset</b>	<b>CC</b>	<b>FP</b>	<b>FN</b>	<b>SE</b>	<b>SP</b>	<b>PPV</b>	<b>NPV</b>
<b>4</b>	95.39	2.13	56.16	43.84	97.87	49.78	97.31
<b>5</b>	93.89	3.03	59.27	40.73	96.99	44.04	96.57
<b>6</b>	96.30	1.05	63.41	36.59	98.95	60.66	97.24
<b>11</b>	95.96	2.09	53.31	46.69	97.91	46.98	97.89
<b>12</b>	93.48	5.36	54.47	45.53	94.85	20.06	98.39

Figure 5.5 through 5.7 show the axial image slices with respect to different sequences after morphological operations. T1 DUAL and THRIVE sequences give better results after morphological operations. However, erosion step causes quite many losses in the pixels of the liver. Therefore, only the connected component is used as a morphological operation in T1 WATS sequences. Tables 5.5, 5.6, and 5.7 give the Symmetric Surface Distance (SSD) metric results after morphological operations (Heimann et al., 2009).

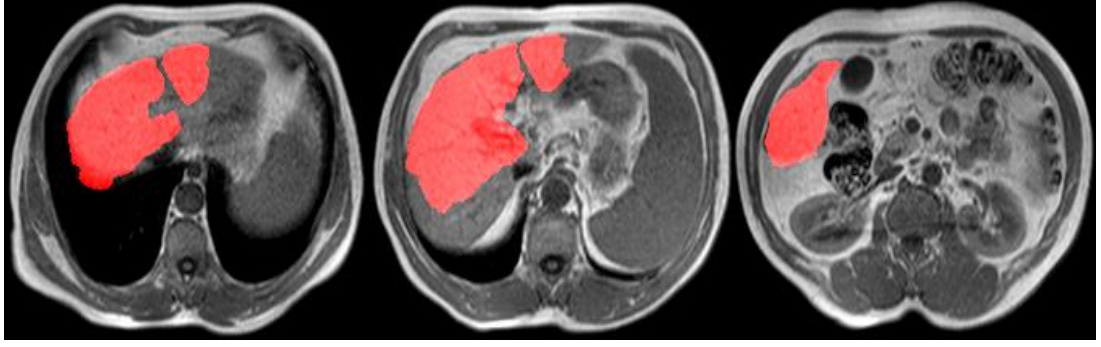


Figure 5.5 Different axial image slices belonging to T1 DUAL after morphological operations.

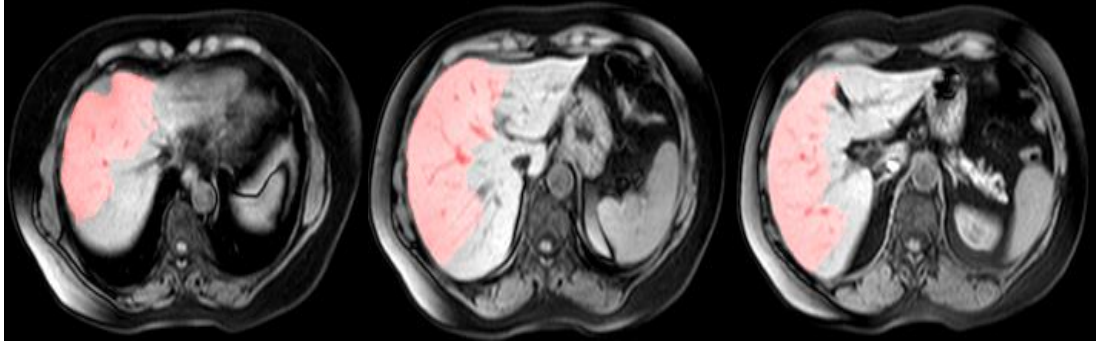


Figure 5.6 Different axial image slices belonging to T1 WATS after morphological operations.

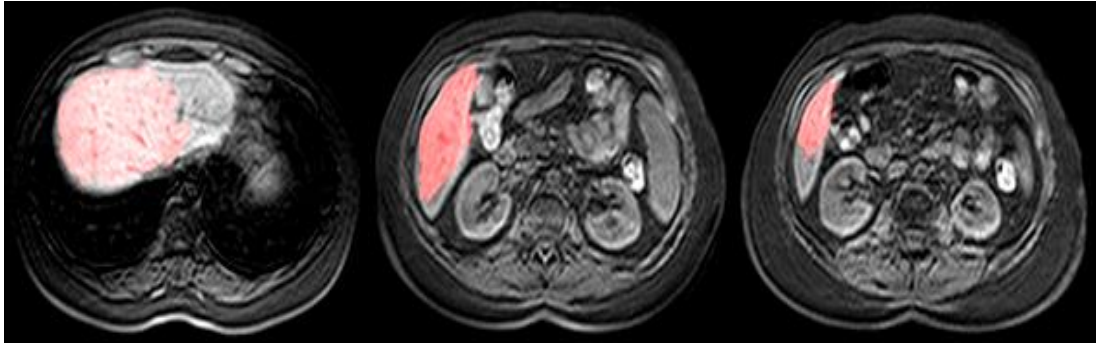


Figure 5.7 Different axial image slices belonging to THRIVE after morphological operations.

In the evaluation of the results, besides the difference in volume values, conformational characteristics of the obtained segmentation results are also important. For this purpose, SSD, which is a widely used metric, is also used for performance evaluations. SSD metric allows the comparison of segmented 3-D organ with the reference 3-D organ by using surface voxels of a 3-D object. The voxels which are known as surface voxels are defined according to at least one voxel that does not belong to the object in 18 possible neighboring. For each surface voxel in the reference organ ( $V_R$ ), the distance to the surface voxel in the segmented organ is calculated according to the Euclidean Distance Metric. The smallest distance among

the measured distances is determined by the nearest neighbor rule. If surface voxels of the segmented organ ( $V_S$ ) are defined as  $S(V_S)$ , the distance of any voxel ( $v_r$ ) in the  $V_R$  to  $S(V_S)$  is calculated as:

$$d(v_r, S(V_S)) = \min_{\substack{v \in S(V_R) \\ \forall q \in S(V_S)}} (\|v_r - q\|) \quad (5.2)$$

To obtain the symmetry characteristic, the same procedure is repeated for any surface voxel ( $v_s$ ) of the segmented organ and the surface voxels which belong to  $V_R$  ( $d(v_s, S(V_R))$ ). Three SSD metrics are calculated as:

Average Symmetric Surface Distance (ASSD):

$$\begin{aligned} ASSD(V_R, V_S) = \\ \frac{1}{|S(V_S)| + |S(V_R)|} (\sum_{v_r \in S(V_R)} d(v_r, S(V_S)) + \sum_{v_s \in S(V_S)} d(v_s, S(V_R))) (mm) \end{aligned} \quad (5.3)$$

RMS Symmetric Surface Distance (RSSD):

$$\begin{aligned} RSSD(V_R, V_S) = \\ \frac{1}{|S(V_S)| + |S(V_R)|} (\sum_{v_r \in S(V_R)} d^2(v_r, S(V_S)) + \sum_{v_s \in S(V_S)} d^2(v_s, S(V_R))) (mm) \end{aligned} \quad (5.4)$$

Maximum Symmetric Surface Distance (MSSD):

$$\begin{aligned} MSSD(V_R, V_S) = \\ \max\{\max_{v_r \in S(V_R)}\{d(v_r, S(V_S))\}, \max_{v_s \in S(V_S)}\{d(v_s, S(V_R))\}\} (mm) \end{aligned} \quad (5.5)$$

$|S(V_S)|$  and  $|S(V_R)|$  give the number of voxels which are in  $V_S$  and  $V_R$ , respectively.

Table 5.5 Metric results of T1 DUAL sequence after morphological operations with respect to the dataset

<b>Dataset</b>	<b>ASSD</b>	<b>RSSD</b>	<b>MSSD</b>	<b>AHO</b>	<b>VHO</b>
<b>3</b>	3.86	7.48	36.07	35.51	36.82
<b>4</b>	4.26	7.06	30.13	55.62	57.30
<b>5</b>	2.33	3.20	15.56	40.86	35.99
<b>6</b>	2.81	4.06	19.24	68.08	54.72
<b>7</b>	4.58	10.13	57.74	57.00	43.69
<b>10</b>	2.72	4.43	24.45	27.25	26.39
<b>11</b>	2.88	5.64	33.75	57.12	43.53
<b>12</b>	3.83	8.21	39.17	34.73	34.12
<b>13</b>	4.30	8.06	43.87	60.06	53.42
<b>16</b>	2.54	3.85	22.65	52.34	43.16
<b>18</b>	2.73	3.95	20.69	77.82	54.99
<b>19</b>	5.09	11.10	54.12	42.34	38.00
<b>21</b>	5.98	10.22	48.51	91.80	58.83
<b>Ave</b>	3.69	6.72	34.30	53.89	44.69

Table 5.6 Metric results of T1 WATS sequence after morphological operations with respect to the dataset

<b>Dataset</b>	<b>ASSD</b>	<b>RSSD</b>	<b>MSSD</b>	<b>AHO</b>	<b>VHO</b>
<b>2</b>	1.78	4.04	28.18	21.26	20.65
<b>3</b>	4.65	9.93	49.41	34.82	38.24
<b>7</b>	7.02	12.10	49.30	64.99	60.79
<b>10</b>	17.39	22.60	63.17	105.61	97.38
<b>16</b>	3.80	7.12	36.28	37.86	37.74
<b>17</b>	3.02	5.70	36.41	43.27	41.64
<b>18</b>	9.16	14.08	47.19	74.19	73.06
<b>19</b>	5.87	12.11	59.14	39.22	39.33
<b>20</b>	4.02	9.42	48.21	33.51	31.29
<b>21</b>	12.78	16.59	47.42	85.70	84.51
<b>Ave</b>	6.95	11.37	46.47	54.04	52.46

Table 5.7 Metric results of THRIVE sequence after morphological operations with respect to the dataset

<b>Dataset</b>	<b>ASSD</b>	<b>RSSD</b>	<b>MSSD</b>	<b>AHO</b>	<b>VHO</b>
<b>4</b>	3.99	5.42	22.56	36.46	36.49
<b>5</b>	7.42	13.25	57.14	43.13	45.62
<b>6</b>	6.16	8.82	32.16	51.28	52.84
<b>11</b>	4.67	7.29	35.89	40.19	38.42
<b>12</b>	8.43	16.30	65.27	43.03	46.94
<b>Ave</b>	6.13	10.22	42.60	42.82	44.06



Figures 5.8 through 5.10 show the axial image slices with respect to different sequences after region growing segmentation method. Tables 5.8 through 5.10 give the SSD metric results after region growing segmentation method. The results seem to be successful, especially in terms of values of ASSD, RSSD, MSSD compared with the literature. Considering the challenges of collecting the image series from daily routine, it is a noteworthy achievement to use these image slices in this study.

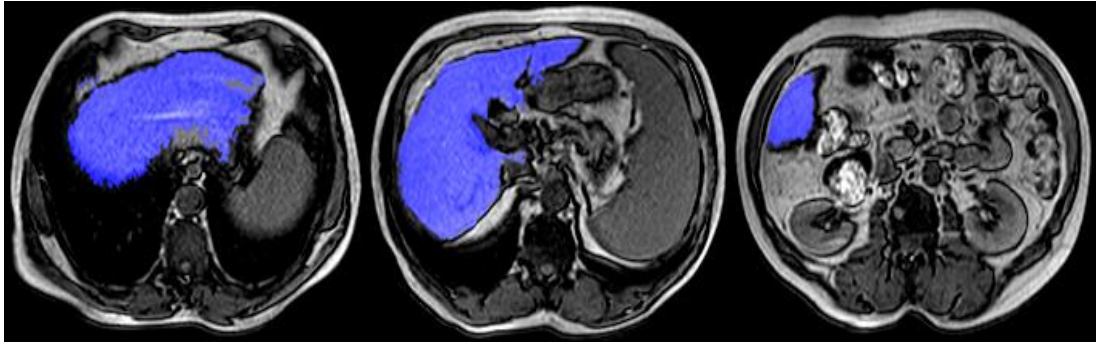


Figure 5.8 Different axial image slices belonging to T1 DUAL after region growing.

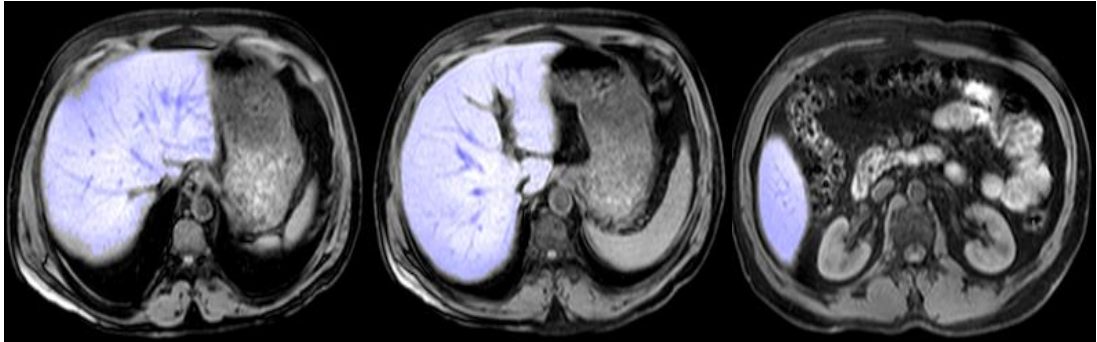


Figure 5.9 Different axial image slices belonging to T1 WATS after region growing.

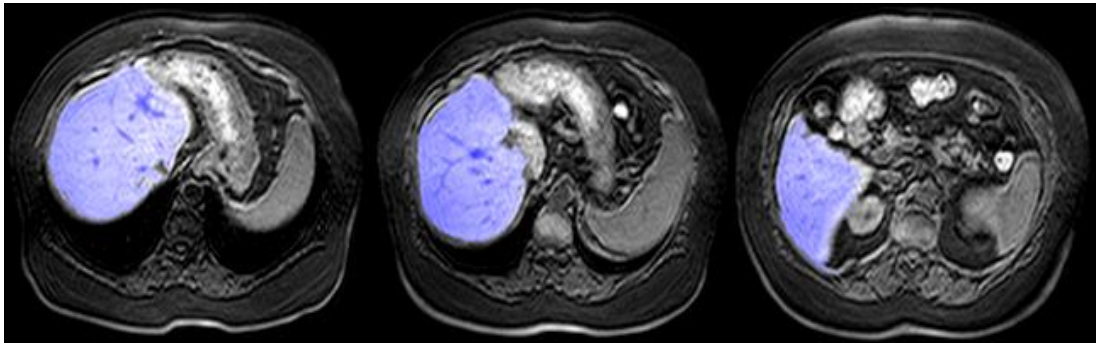


Figure 5.10 Different axial image slices belonging to THRIVE after region growing.

Table 5.8 Metric results of T1 DUAL sequence after region growing with respect to the dataset

<b>Dataset</b>	<b>ASSD</b>	<b>RSSD</b>	<b>MSSD</b>	<b>AHO</b>	<b>VHO</b>
<b>3</b>	0.88	1.44	12.25	19.04	18.35
<b>4</b>	1.69	2.41	13.08	38.63	35.18
<b>5</b>	1.09	1.70	10.86	22.37	19.19
<b>6</b>	1.31	1.94	9.27	35.61	28.82
<b>7</b>	2.34	3.12	14.04	65.35	47.63
<b>10</b>	1.30	1.76	10.39	19.24	17.60
<b>11</b>	10.10	20.74	84.37	75.33	60.98
<b>12</b>	3.12	7.44	47.48	24.89	23.24
<b>13</b>	1.40	2.12	27.75	34.23	30.86
<b>16</b>	1.21	1.56	8.54	34.61	27.99
<b>18</b>	16.29	29.12	109.75	130.34	83.42
<b>19</b>	1.74	3.61	39.22	39.51	23.75
<b>20</b>	7.01	11.97	76.64	193.42	107.15
<b>21</b>	4.82	6.83	29.27	106.46	64.28
<b>Ave</b>	3.88	6.84	35.21	59.93	42.03

Table 5.9 Metric results of T1 WATS sequence after region growing with respect to the dataset

<b>Dataset</b>	<b>ASSD</b>	<b>RSSD</b>	<b>MSSD</b>	<b>AHO</b>	<b>VHO</b>
<b>2</b>	1.27	1.81	14.87	35.21	25.71
<b>3</b>	1.27	1.76	11.75	29.82	26.90
<b>7</b>	1.71	2.26	12.65	50.03	36.67
<b>10</b>	2.92	3.80	14.90	33.99	33.31
<b>16</b>	1.49	2.03	13.45	33.82	30.29
<b>17</b>	1.46	2.29	19.00	34.01	28.99
<b>18</b>	1.25	2.01	13.00	25.58	24.94
<b>19</b>	0.78	1.62	19.44	13.87	11.66
<b>20</b>	2.56	4.59	49.46	49.32	40.94
<b>21</b>	2.61	3.92	18.97	30.43	27.55
<b>Ave</b>	1.73	2.61	18.75	33.61	28.70

Table 5.10 Metric results of THRIVE Sequence after region growing with respect to the dataset

<b>Dataset</b>	<b>ASSD</b>	<b>RSSD</b>	<b>MSSD</b>	<b>AHO</b>	<b>VHO</b>
<b>4</b>	2.97	3.76	14.14	31.15	29.75
<b>5</b>	3.75	5.23	22.09	35.95	34.06
<b>6</b>	3.78	4.69	15.56	37.81	36.53
<b>11</b>	2.45	3.02	15.07	27.29	26.10
<b>12</b>	1.91	3.16	21.59	15.91	16.13
<b>Ave</b>	2.97	3.97	17.69	29.62	28.51



A general comparison of average metric results obtained after region growing for all the datasets used is given in Table 5.11.

Table 5.11 Comparison of the average metric results of all sequences after region growing

<b>Dataset</b>	<b>ASSD</b>	<b>RSSD</b>	<b>MSSD</b>	<b>AHO</b>	<b>VHO</b>
<b>T1 DUAL</b>	3.88	6.84	35.21	59.93	42.03
<b>T1 WATS</b>	1.73	2.61	18.75	33.61	28.70
<b>THRIVE</b>	2.97	3.97	17.69	29.62	28.51

## 5.1 General Overview

As described in detail in Chapter 4, our proposed method and the Transfer Function (TF) techniques which are discussed in the literature section share the same strategy (coarse + fine approximation). The proposed new two-step strategy for the TF design implements user defined VHS approximation initially by using multi-scale hierarchical model and the ensuing refinement by using local tissue information. We have the following observations:

- 1) Our study introduces a new intuitive multi-dimensional TF domain. With the help of the user defined MPR GUI, new image slices are constructed by determining the major axis/region. By aligning the histograms of the new image slices of MR series, VHS can be obtained.
- 2) The application of multi-scale and hierarchical Gaussian Mixture Model strategy is improved. Our model can fit and classify the organ of interest automatically and in real time.
- 3) Based on spatial and morphological operations, the performance metrics of the organ of interest are increased.
- 4) The performance measurement of our approach is performed by applying it to various and multiple clinical abdominal MRI datasets with different sequence protocols.

## **CHAPTER SIX**

### **CONCLUSION**

MRI acquisitions create volumetric data which is usually in the form of a series of cross sections of the anatomy of interest. The visualization of this volumetric medical data has several benefits such as surgery planning and treatment follow-ups. Therefore, it is more preferable for applications that require more effective and intuitive visualizations. The visualization of 3-D data along with slice-by-slice evaluation can help many scientific disciplines. Convenience and effectiveness of dealing with 3-D data comes at the expense of some complexity in the visualization. Some recent studies are interested in dealing with the complexity of rendering and visualization. One of the most important points is to give accurate and clear information in medical visualization. Therefore, defining a transfer function (TF) is one of the most important and complex steps in the generation of volume rendered medical visualizations. Optical parameters such as opacity and color must be determined as a crucial step to construct a valuable outcome in rendering.

The difficulty of TF design can be significantly reduced with effective initial designs, which provide a starting point prior to the optimization that is controlled by the user. To overcome the difficulty of initial TF generation, a semi-automatic method is introduced in this thesis work. Our approach is based on a volume histogram stack (VHS), which is created by aligning the histograms of the image slices of MR series. Thanks to the VHS, the organ of interest can be distinguishable by using inter-slice spatial domain knowledge. The change in the gray levels can be revealed through the series of slices.

Before aligning slices, we present a new graphical user interface (GUI) which constructs new images using different anatomical planes. By using this GUI, we can understand and display tissues which are not seen well in the original images. The multi-planar reconstruction (MPR) technique is an accessible tool that can replace or complement more conventional imaging approaches. Evaluating this reconstruction approach in abdominal MR images serves a wide variety of pathological processes.

The multi-planar reconstruction programs can also expand a radiologist's capacity to define pathologies.

Dealing with different surfaces in the construction of an MPR image allows us to gather information about lobes, which are suppressed by any other unwanted components. Working with one axis only cannot segment the desired lobe if it is a minor lobe in the VHS. The main reason of constructing VHS is to differentiate gray levels of the organ of interest. By changing the perspective of volumetric data, any desired part of the VHS can be emphasized and segmented by different approximations. In our study, we use different anatomical planes with the help of our GUI and obtain new slices which form the input data of the VHS.

The resultant VHS, which is produced by the GUI, and their desired (labeled by an expert) counterparts are compared in the previous sections. Considering the general VHS structure and comparing the actual VHS with the desired VHS shows that Gaussian functions could be good approximations. MRI has a challenging structure so that its intensity fluctuations cause a non-smooth structure in the VHS. The major problem is the variety in the gray level of the same organ among slices which causes discontinuities in the VHS. Another problem is the slice thickness between two slices which is wide enough to cause a limited sampling in  $z$ -direction. This problem causes an incompatibility in the size of VHS in the form that dimensions along  $x$  and  $y$  axes are considerably different. By taking these problems into account, Gaussian functions are considered to be good candidates which can provide an approximation of the TF. In this study, by considering these criteria, a hierarchical and multi-scale modeling is proposed. In an iterative manner, the proposed model tries to find the best Gaussian basis to fit the corresponding part of the VHS. The developed algorithm provides a procedure for capturing all suppressed lobes of importance in a successive manner by associating the lobes with a suitable number of Gaussian bases.

The desired histogram is separated from the unwanted components/tissues after fitting Gaussian functions with two valleys in both sides of it. In our study, by taking

an advantage of this distinction, we use a thresholding method. Our main aim is to determine two threshold values which correspond to the valleys at the left and right side of the corresponding lobes of the organ of interest. The important point is the adjustable structure of this thresholding method. The threshold ranges are determined through the VHS, which corresponds to all images and extends toward the tails of the Gaussian functions. The variety in the shape and size of the organ of interest could affect VHS directly. The special appearance of VHS dictates employment of a dynamic threshold rather than a fixed one. Considering the error rates, in the middle slices of the image series, we can obtain sufficiently high success in the segmentation of the desired lobe from the VHS.

This approximation is even further optimized using morphological operations of erosion and dilation and region growing. The obtained final classification results fulfil our aim of segmenting the organs of interest via the MR sequences belonging to the challenging abdominal region of the body.

## REFERENCES

- Antoine, J. – P. & Murenzi, R. (1996). Two-dimensional directional wavelets and the scale-angle representation. *Signal Processing*, 52, 259-281.
- Bae, K. T., Giger, M. L., Chen, C. T., & Jr. Kahn, C. E. (1993). Automatic segmentation of liver structure in CT images. *Medical Physics*, 20, 71-78.
- Bidaut, L. (2000). Data and image processing for abdominal imaging. *Abdominal Imaging*, 25, 341–360.
- Brown, M. A. & Semelka, R.-C. (1999). MR imaging abbreviations, definitions, and descriptions: A review. *Radiology*, 213, 647-662.
- Castro, S., König, A., Löffelmann, H., & Gröller, E. (1998). Transfer function specification for the visualization of medical data. *Austria Vienna University of Technology Technical Report*.
- Chan, T. F. & Vese, L. A. (2002). Active contours without edges. *IEEE Transactions Medical Imaging*, 10, 266-277.
- Chen, G., Gu, L., Qian, L., & Xu, J. (2009). An improved level set for liver segmentation and perfusion analysis in MRIs. *IEEE Transactions on Information Technology in Biomedicine*, 13, 94-103.
- Drebin, R. A., Carpenter, L., & Hanrahan P. (1988). Volume rendering. *Computer Graphics*, 22, 65-74.
- Efford, N. (1st edt.) (2000). *Digital imaging processing: A practical introduction using Java<sup>TM</sup>*. Pearson.

- Flohr, T. G., Schaller, S., Stierstorfer, K., H. Bruder, H., Ohnesorge, B. M., & Schoepf, U. J. (2005). Multi detector row CT systems and image reconstruction techniques, *Radiology*, 235, 756–773.
- Ginneken, B. V., Heiman, T., & Styner, M. (2007). 3-D segmentation in the clinic: A grand challenge. *MICCAI Workshop Proceedings*, 7-15.
- Heimann. T., van Ginneken. B., Styner. M. A., Arzhaeva. Y., Aurich. V., Bauer, C., et al. (2009). Comparison and evaluation of methods for liver segmentation from CT datasets. *IEEE Transactions on Medical Imaging*, 28, 1251-1265.
- Hermoye, L., Azjal, I. L., Cao, Z., Annet, L., Lerut, J., Dawant, B. M., et. al. (2005). Liver segmentation in living liver transplant donors: Comparison of semiautomatic and manual methods. *Radiology*, 23, 171-178.
- Hoa, D. (n.d.). *Characteristics of an MRI Sequence*, Retrieved April, 2014 from <http://www.imaio.com/en/e-Courses/e-MRI/MRI-Sequences/sequence-characteristics>
- Hornak, J. P. (n.d.). *The basics of MRI*, Retrieved June, 2014 from <http://www.cis.rit.edu/htbooks/mri/inside.htm>
- Irani, M. & Peleg, S. (1991). Improving resolution by image registration. *CVGIP: Graphical Models and Image Processing*, 53, 231-239.
- Jain, A. K., Jianchang, M., & Mohiuddin K. M. (1996). Artificial neural networks: A tutorial. *IEEE Computer Society*, 29, 31-44.
- Kellberg, J., Karlsson A.-K., Stokland E., Svensson P.-A., & Dahlgren J. (2010). Adipose tissue distribution in children: Automated quantification using water and fat MRI. *Journal of Magnetic Resonance Imaging*, 32, 204-210.

- Kindlman, G. & Durkin, J. W. (1998). Semi-automatic generation of transfer functions for direct volume rendering. *VVS '98 Proceedings of the 1998 IEEE Symposium on Volume Visualization*, 79-86.
- Kniss, J., Kindlmann, G., & Hansen, C. (2002). Multidimensional transfer functions for interactive volume rendering. *Visualization and Computer Graphics*, 8, 270–285.
- Koss, J. E., Newman, F. D., Johnson, T. K., & Kirch, D. L. (1999). Abdominal organ segmentation using texture transforms and a Hopfield neural network. *IEEE Transaction Medical Imaging*, 18, 640–648.
- König, A. H. & Gröller, E. M. (2001). Mastering function specification by using VolumePro technology. *Spring Conference on Computer Graphics*, 17, 279-286.
- Lee, C. C., Chung, P. C., & Tsai, H. M. (2003). Identifying multiple abdominal organs from CT image series using a multi-module contextual neural network and spatial fuzzy rules. *IEEE Transactions on Information Technology in Biomedicine*, 7, 208–217.
- Levoy, M. (1988). Display of surfaces of volume data. *IEEE Computer Graphics & Applications*, 8, 29-37.
- Lundström, C., Ljung, P., & Ynnerman, A., (2006a). Extending and simplifying transfer function design in medical volume rendering using local histograms. *Proceedings Eurographics/IEEE-VGTC Symposium*, 227-234.
- Lundström, C., Ljung, P., & Ynnerman, A., (2006b). Local histograms for design of transfer functions in direct volume rendering. *IEEE Transactions Visualization and Computer Graphics*, 12, 1570-1579.

*Magnetic Resonance Imaging (MRI) – Body*. (May 9, 2013). Retrieved June, 2014 from <http://www.radiologyinfo.org/en/pdf/bodymr.pdf>

McRobbie, D. W., Moore, E. A., Graves, M. J., & Prince, M. R. (2003). *MRI: From picture to proton*. (2nd ed.). Cambridge: Prince.

Pfister, H., Lorensen, B., Bajaj, C., Kindlmann G., Schroeder, W., Avila, L. S., et al. (2001). Visualization viewpoints: The transfer function bake-off. *IEEE Computer Graphics & Applications*, 21, 16-22.

Pfister, H., Lorensen, B., Bajaj, C., Kindlmann, G., Schroeder W., & Machiraju R. (2000). The transfer function bake-off. *Proceedings 11th IEEE Visualization Conference*, 11, 523-526.

Prince, J. P., & Links, J. M. (1st ed.). (2006). *Medical imaging signals and systems*. New Jersey: Pearson.

Sabella, P. (1988). A rendering algorithm for visualizing 3D scalar fields. *Computer Graphics*, 22, 51-58.

Selver, M. A., & Güzeliş, C. (2009). Semiautomatic transfer function initialization for abdominal visualization using self-generating hierarchical radial basis function networks. *IEEE Transactions on Visualization and Computer Graphics*, 15, 395-409.

Selver, M. A., Kocaoğlu, A., Demir, G., Doğan, H., Dicle, O., & Güzeliş, C. (2008). Patient oriented and robust automatic liver segmentation for pre-evaluation of liver transplantation. *Computers in Biology and Medicine*, 38, 765-784.

Selver, M. A., Özdemir, M., & Selvi, E. (2013). Interactive radial volume histogram stacks for visualization of kidneys from CT and MRI. *International Conference in*



*Central Europe on Computer Graphics Visualization and Computer Vision*, 21, 233-242.

Seo, K. S., Kim, H.-B., Park, T., Kim, P.-K., & Park, J.-A. (2005). Automatic liver segmentation of contrast enhanced CT images based on histogram processing. *Advances in Natural Computation Lecture Notes in Computer Science*, 3610, 1027-1030.

Seo, K. S., Ludeman, L. C., Park, S. J., & Park, J. A. (2004). Efficient liver segmentation based on the spine. *Lecture Notes in Computer Science*, 3261, 400-409.

Upson, C., & Keeler, M. (1988). V-buffer: Visible volume rendering. *SIGGRAPH'88 Proceeding of the 15<sup>th</sup> Annual Conference on Computer Graphics and Interactive Techniques*, 59-64.

Westbrook, C. (2008). *Handbook of MRI technique*. (3rd ed.). Oxford, United Kingdom: Wiley-Blackwell

Westbrook, C. (2002). *MRI at a glance*. (1st ed.)., England: Blackwell Science.

Westbrook, C. & Kaut, C. (1998). *MRI in practice*. (4th ed.)., England: Blackwell Science.

Wink, A. M. & Roerdink, J. B. T. M. (2004). Denoising functional MR images: A comparison of wavelet denoising and Gaussian smoothing. *IEEE Transaction Medical Imaging*, 23, 374-387.